



HAL
open science

PETROACOUSTIC CHARACTERIZATION OF FRACTURED LIMESTONES FROM THE VADOSE ZONE OF BEAUCE AQUIFER (O-ZNS, France)

Abdoul Nasser Yacouba, Céline Mallet, Jacques Deparis, Kévin Beck, Gautier
Laurent, Philippe Leroy, Mohamed Azaroual, Damien Jougnot

► **To cite this version:**

Abdoul Nasser Yacouba, Céline Mallet, Jacques Deparis, Kévin Beck, Gautier Laurent, et al..
PETROACOUSTIC CHARACTERIZATION OF FRACTURED LIMESTONES FROM THE VA-
DOSE ZONE OF BEAUCE AQUIFER (O-ZNS, France). 2024. hal-04520290

HAL Id: hal-04520290

<https://hal.science/hal-04520290>

Preprint submitted on 25 Mar 2024

HAL is a multi-disciplinary open access archive for the deposit and dissemination of scientific research documents, whether they are published or not. The documents may come from teaching and research institutions in France or abroad, or from public or private research centers.

L'archive ouverte pluridisciplinaire **HAL**, est destinée au dépôt et à la diffusion de documents scientifiques de niveau recherche, publiés ou non, émanant des établissements d'enseignement et de recherche français ou étrangers, des laboratoires publics ou privés.



Distributed under a Creative Commons Attribution - NonCommercial - NoDerivatives 4.0
International License



PETROACOUSTIC CHARACTERIZATION OF FRACTURED LIMESTONES FROM THE VADOSE ZONE OF BEAUCE AQUIFER (O-ZNS, France)

Abdoul Nasser Yacouba^{1,2*}, Céline Mallet^{1*}, Jacques Deparis², Kévin Beck³, Gautier Laurent¹, Philippe Leroy², Mohamed Azaroual^{1,2}, Damien Jougnot⁴

¹ ISTO, UMR 732, Univ Orleans, CNRS, BRGM, OSUC, F-45071 Orleans, France

² French geological survey, BRGM, F-45100, Orleans, France

³ Univ. Orleans, Univ. Tours, INSA-CVL, LaMé EA7494, 8 rue Léonard de Vinci, F-45072 Orleans, France

⁴ Sorbonne Université, CNRS, EPHE, UMR 7619 METIS, F-75005 Paris, France

ABSTRACT

Fluid flow in reservoir rocks are mainly controlled by heterogeneities present at all scales, especially for carbonate reservoirs. Predicting reservoir and acoustic properties becomes tremendously difficult in complex environments like vadose zone. We investigated petroacoustic properties coupled to macroscopic descriptions of limestone samples from the Beauce aquifer vadose zone of the O-ZNS observatory (Villamblain, France). At first sight, the different samples present highly heterogeneous features defined as macropores (fractures, cracks, dissolution vugs). The petrophysical characterization shows that the reservoir properties are scattered for the samples with important macropores resulting in a poor permeability-porosity relationship. However, the permeability prediction is improved by using pore size as a second controlling factor. Indeed, it is the case for different samples with micritic matrices associated with more or less non-connected micropores. The velocity-porosity correlation and relationship with empirical models shows correlated relations allowing to differentiate samples with respect to their structures. However, we highlighted that the presence of macropores tends to minimize the control of the effective porosity. The influence of density on velocities is very difficult to establish and none of the empirical models allow a satisfying estimation. Finally, applying petroacoustic models highlights a close relationship between the presence of macropores and the dispersion of reservoir and elastic properties.

Key words

Petrophysics, Acoustics, Fractured limestones, Vadose zone



1 INTRODUCTION

The critical zone is the external layer of the Earth's crust where water, gases, and minerals interact with living beings to produce soil, sediments and nutrients (National Research Council, 2001). It is characterized by its multiple processes, resulting in a complex ecosystem. The vadose zone refers to the partially water saturated zone, located within the critical zone between the soil surface and the water table. The complex vadose zone plays crucial role in water resources monitoring and management (Stephens, 1996).

To characterize fluid flow involved in the recovery and the recharge of these resources, permeability and porosity are the key petrophysical parameters (Bourbié et al., 1992). Porosity represents the volume of voids over the total volume of the rock whereas permeability defines the ability of a rock to allow a fluid circulation through it (Bernabé & Mainault, 2015). The porosity connectivity and pathways for fluid flow is expected to be the first controlling parameter of permeability. However, it is not always the case for complex sedimentary rocks, especially in carbonates. Indeed, these two properties are the result of long-term sedimentary, tectonic, and diagenetic processes conferring them storage and delivering capabilities for different fluids (Chilingar, 1964; Moore & Wade, 2002; United Nations, 2022). Thus, the overall permeability-porosity relations and the fluid flow are controlled by the multi-scale geological and structural heterogeneities in sedimentary rocks (Yu et al., 2018). These heterogeneities are defined by the granulometry, the pore geometry (size, distribution, tortuosity and constrictively) and the presence of fractures. They are present at all scales (micro, meso and macroscopic), especially in carbonates (Dominguez et al., 1992; Lucia, 2007). Depending on the scale, these heterogeneities do not have the same influence on the porosity-permeability pattern (Berg, 1970; Bloch, 1991; Nelson, 1994; Lucia, 1995), which calls for adequate investigation methods (Archie, 1950; Tiab & Donaldson, 2015).

More often, to be integrated into reservoir models, these petrophysical properties are estimated at field scale using geophysical techniques such as electrical, magnetic or seismic methods (Lake, 2012; Binley et al., 2015). These methods, can provide indirect access to important petrophysical parameters with relatively good resolution in 2D, 3D, or 4D (Kearey et al., 2002; Fan et al., 2020; Hermans et al., 2023). However, they are often accompanied by uncertainties for reservoir properties inversion and interpretation that must be calibrated and quantified in the laboratory by petrophysical models (Bosch et al., 2010; Rasolofosaon & Zinszner, 2004). Among the geophysical methods, the acoustic method is well suited for reservoir characterization as there is a strong link between transport and elastic properties (Mavko et al., 1998). Elastic waves are indeed very sensitive to the internal structure of the rock material especially the pore structure (Guéguen et al., 2009; Germán Rubino et al., 2013). Reservoir characterization based on petroacoustic modelling has been discussed for several decades. Pioneer studies based on well and laboratory data, have proposed empirical petroacoustic models, which actually serve as a reference in the scientific community (Wyllie et al., 1956; Gardner et al., 1974; Raymer et al., 1980; Greenberg & Castagna, 1992). These models are often limited to homogenous systems with a simple porosity system. For silico-clastic reservoirs, much more adapted models can be found in the literature (Castagna et al., 1985; Han et al., 1986; Vernik & Nur, 1992). For carbonate rocks, however, the task is more difficult, although there are many works that propose empirical petroacoustic models linking acoustic velocities to porosity (Rafavich et al., 1984; Wang et al., 1991; Anselmetti & Eberli, 1993; Palaz & Marfurt, 1997; Baechle et al., 2000; Weger et al., 2009), to permeability (Fabricius et al., 2007) or to the rock fabric (Anselmetti & Eberli, 1993; Fabricius et al., 2010; Fournier et al., 2011; Regnet et al., 2015; Bailly et al., 2022). Indeed, carbonate reservoirs, in particular lacustrine limestones due to their geological history, are more complex and heterogeneous in terms of texture and microstructures

1 than silico-clastic reservoirs (Moore & Wade, 2002; Tucker & Wright, 2009; Regnet et al.,
2 2019). These heterogeneities are enhanced by diagenetic processes and weathering in complex
3 environments like the vadose zone, making reservoir and acoustic properties prediction
4 uncertain.

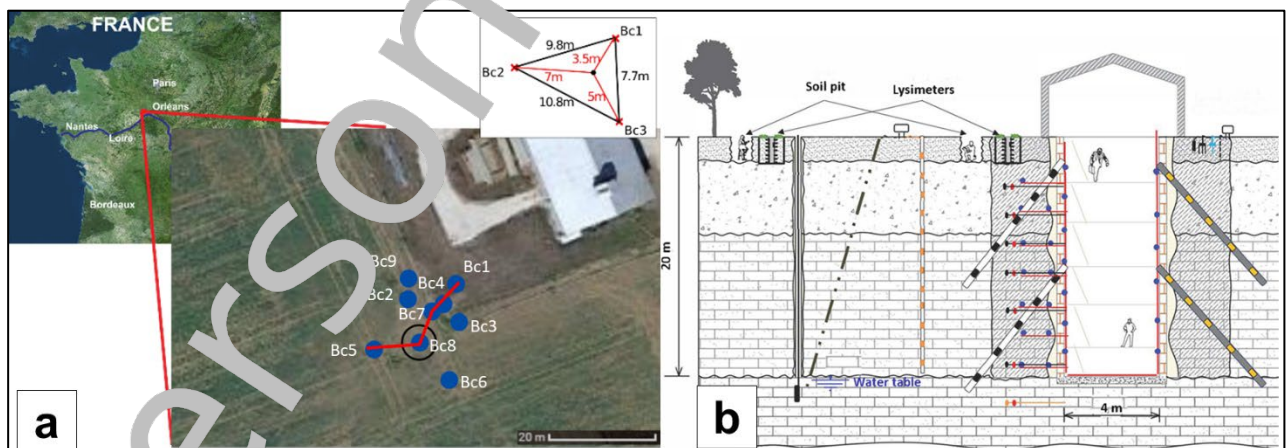
5 The objectives of this paper are (i) to combine rock structure heterogeneities and petro-acoustic
6 properties in order to model and predict the structure of different limestones facies in complex
7 settings, and (ii) to infer the influence of the fracturing on both reservoir and elastic properties
8 at laboratory scale. To this aim, the present approach combines petrophysical (porosity, density,
9 permeability and acoustic velocities) measurements, and macroscopic observations on
10 limestones samples from the O-ZNS platform (standing for “Observatoire des transferts dans
11 la Zone Non Saturée”, in French). Based on these measurements, the emphasis is first placed
12 on the reservoir properties characterization in order to develop permeability-porosity models
13 adapted to our samples. Then, we analyze the acoustic behavior of these limestones and finally
14 discuss their controlling factors through petroacoustic models.

15 2 MATERIAL AND METHODS

16 2.1 Study site and geological context

17 The vadose zone of Beauce aquifer is an extremely complex porous and fractured medium. Its
18 study requires the complementarity of various disciplines. To tackle this challenge, the O-ZNS
19 platform is set-up at Villamblain (Loiret, France). It is composed by a main well of 20 m-depth
20 and 4 m-diameter and 9 cored boreholes (Figure 1). It adopts an innovative multidisciplinary
21 and multi-scale approach to assess and monitor the Beauce aquifer and characterize the heat
22 and mass transfers through its vadose zone. Various ongoing research projects from diverse
23 disciplines are applied to O-ZNS characterization such as hydrology (Aldana et al., 2021; Isch
24 et al., 2022), geomechanics (Mallet et al., 2022a), site instrumentation (Abbar et al., 2022),
25 geophysics (Abbas et al., 2022 ; Mallet et al., 2022b), geology and digital outcrop modelling
26 (Laurent et al., 2023).

27



28
29 Figure 1. A) Location map of the O-ZNS platform with the location of the different boreholes (Bc).
30 The black circle shows the location of the main well made after the boreholes and destroying
31 Bc9. The red line is the well-well correlation line used for Figure 2. B) Sketch of the main well
32 with the surface instrumentation and future boreholes (Abbar et al., 2022).

33

1 The Beauce Limestones formation is one of the four major carbonate platform of the Paris
2 Basin, namely the Grossier, Saint-Ouen, Brie, and Beauce. The Beauce Limestones formation
3 is a lacustrine to palustrine formation, deposited from the end of the Oligocene (34-23 Ma) to
4 the beginning of the Miocene (Aquitainian: 23-20 Ma) with the withdrawal of the Tethyan Sea
5 (Ménillet & Edwards, 2000). Located in the south of the Paris Basin, the Beauce Limestones
6 formation occupies a large area with an extension of 160 km from North to South and 130 km
7 from East to West (Lorain, 1973). This formation has undergone minor tectonic episodes
8 resulting in very localized structures and probable fractures. However, it has undergone several
9 periods of erosion and weathering (both chemical and mechanical) which lead to important
10 fissuration, karstification and mineral transformation. At Villambert (O-ZN site), the Beauce
11 Limestone formation starts around 2 m deep (with a unit known as the Pithiviers Limestones)
12 and reaches up to 25 m. It is underlain by a marly to siliciclastic unit known as the Molasse du
13 Gâtinais, also part of the Beauce Limestones formation (Ménillet & Edwards, 2000). The
14 current level of the water table varies between 17 and 20 m deep, depending on the season
15 (Aldana et al., 2021).

16 The Beauce Limestones formation is very heterogeneous in terms of lithofacies and rock fabric
17 with great lateral and vertical variabilities making the distinction between lithofacies very
18 complex. Ménillet & Edwards (2000) define two main primary lithologies consisting of
19 cemented micrite and microsparites (beige in color) and micrites (grey to dark grey in color)
20 which are very abundant depending on the lithofacies. These rock fabrics show that the Beauce
21 Limestones is globally mud supported limestones. Furthermore, based on drillings and previous
22 works on Beauce Limestones, Trautmann (1974) groups the numerous lithofacies into families
23 including carbonate lithofacies and alteration/dissagregation lithofacies. In the carbonate
24 lithofacies, we find compact, fine-grained beige to yellowish limestones and heteromorphic
25 limestones mainly brecciated limestones.

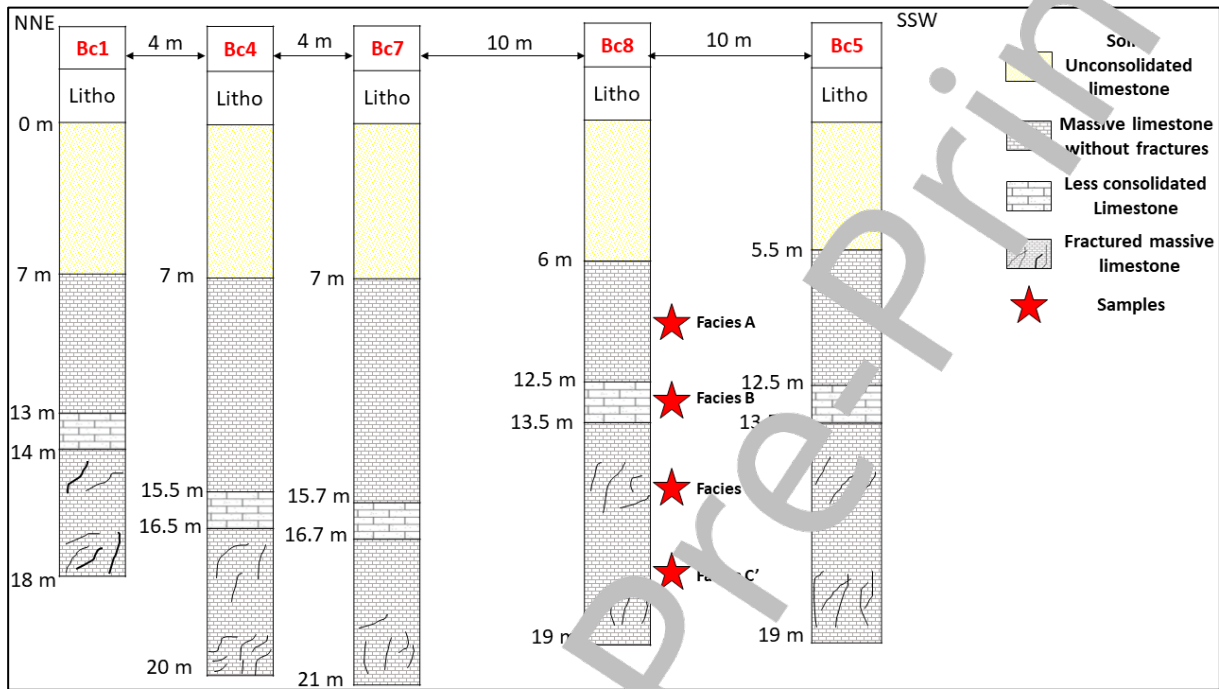
26 2.2 Sample selection

27 In the boreholes, well logs have been acquired including electrical resistivity, neutron, density,
28 caliper, direct imagery and radioactivity logs, summarized by Mallet et al., (2022b). According
29 to these logs and based on the analysis of their variations, we identified two layers. A first layer
30 corresponding to the soil and the unconsolidated (powdery) limestones located between 0 to 7
31 m deep and a second layer below corresponding to the consolidated limestones on which we
32 focus this study. To assess the geological lateral continuity of the investigated formation, a
33 well-well correlation using several boreholes has been proposed (Figure 2). On this well-well
34 correlation, we noticed that the soil and unconsolidated limestones layers keep approximatively
35 the same thickness whereas the levels of consolidated limestone vary in thickness over a
36 relatively small distance, implying important lateral heterogeneities. In order to investigate
37 strongly different rock structures, we selected in the consolidated part three different facies.
38 These petrophysical facies were chosen based on the variations of the density, neutron and
39 caliper logs mainly. They are from the top to the bottom:

- 40 • 7-9 m: massive limestone with less/without fractures noted facies A in this study
- 41 • 2.5-15.5 m: less massive/consolidated limestone corresponding to facies B
- 42 • 14-20 m: fractured massive limestone in which the fracture density increases with
43 depth. We chose to select samples at two different depths in order to cover different
44 degree of fracturation. We obtained then a C and C' facies.

45 In total, 24 samples (six per facies) were cored from limestones blocks obtained during the
46 excavation of the main well. The 24 samples are subdivided into 3 groups according to their
47 diameters (1.5, 2.5, and 4 cm-diameters) and the corresponding lengths are given in Table 1.

- 1 Samples of 2.5 and 4 cm diameter were used for porosity, permeability, and acoustic
- 2 measurements and the smallest samples of 1.5 cm diameter were used for mercury porosimetry.
- 3 Table 1 (in appendix) reports the sample code, facies, depth, number, size and the
- 4 characterization method used.



5
6 Figure 2. Well-well correlation based on five boreholes and the depth of different rock type,
7 highlighting the facies selection.

8 9 2.3. Methods

10 Effective porosity and bulk density (hydrostatic weighing)

11 The sample were weighted under three conditions: dry, saturated and immersed in water. Then,
12 we computed the effective porosity ϕ_{eff} (%), the bulk density of the sample, ρ_b (kg/m^3), and
13 the grain density ρ_s following equations (2.1), (2.2) and (2.3).

$$14 \quad \phi_{eff} = \frac{W_{sat} - W_{dry}}{W_{sat} - W_{im}} \quad (2.1)$$

$$15 \quad \rho_b = \rho_w \frac{W_{dry}}{W_{sat} - W_{im}} \quad (2.2)$$

$$16 \quad \rho_s = \rho_w \frac{W_{dry}}{W_{dry} - W_{im}} \quad (2.3)$$

17 where W_{sat} , W_{dry} and W_{im} are the saturated, dry and immersed mass (kg), respectively, and
18 ρ_w is the water density (kg/m^3). Considering the accuracy of the balance (0.001 g), the porosity
19 and the density are known with an accuracy of $\pm 0.5\%$ and $\pm 25 \text{ kg/m}^3$ respectively.

20 Total porosity and pore structure (mercury injection porosimetry)

21 A mercury porosimeter (or mercury injection capillary pressure: MICP) was used to determine
22 porosity, bulk density and grain density of our samples as well as the distribution of their pore
23 sizes. The principle of measurement consists in introducing mercury (a non-wetting fluid)

1 through the pores of the rock by incrementing the injected pressure. The experimental protocol
2 is based on the use of the Autopore IV 9500 device from Micrometrics which allows to
3 investigate pore diameters from 3 nm to 400 μm (Beck & Al-Mukhtar, 2010). A dry sample is
4 introduced into a tube in which vacuum is made thanks to the device (air pressure: 0.4 psia).
5 Then, liquid mercury is injected with increase of pressure until 60000 psia, and the quantity of
6 injected mercury in equilibrium with the pressure variation is automatically recorded according
7 to a predefined computation program. The collected data were used to obtain the porosity, the
8 bulk density on one hand and the pore size distribution curve and the average pore size on the
9 other hand by using the Washburn equation (Webb, 2001).

10 Permeability (steady flow method)

11 The permeability was measured in steady flow condition (API, 1998). It consists of imposing a
12 constant water pressure difference at the inlet of a saturated sample. Then, the flow rate is
13 measured at the outlet. The system is maintained unchanged until it reaches a stationary state.
14 The validity of Darcy's law is verified when a linear relationship between the pressure gradient
15 and the flow rate is obtained, and the equation (2.3) allowed us to compute the intrinsic/absolute
16 permeability, k , in mD ($1 \text{ mD} = 9.8692 \times 10^{-16} \text{ m}^2$). The apparatus used is a non-conventional
17 triaxial cell equipped with volumetric pumps (Aldana et al., 2021).

$$18 \quad \frac{Q}{S} = \frac{k}{\mu} \left[\frac{(\Delta P)}{L} \right] \quad (2.3)$$

19 where Q is the flow rate (m^3/s), S is the cross section of the samples (m^2), μ is the fluid (water)
20 dynamic viscosity (Pa.s), ΔP is the difference of pressure between the inlet and outlet (Pa), and
21 L is the length of the samples (m). Knowing the accuracy of the different pumps (0.15% for
22 pressure and 0.25% for volume) and the uncertainties related to the sample dimensions (0.001
23 m), the uncertainty of the permeability measurement is ± 0.02 mD.

24 Acoustic measurements

25 The measurements were performed with DPR300 Pulser/Receiver device, a Tektronix
26 DPO 20248 oscilloscope and 0.1 MHz piezoelectric transducers designed for P- and S-waves.
27 Acoustic measurements were carried out on each sample in dry and saturated (water)
28 conditions. We picked the first break to get the travel-time in the samples (corrected thanks to
29 aluminum calibration) and knowing their length, the P- and S-wave velocities were deduced
30 from their ratio. By combining the relative uncertainty/accuracy associated with each source of
31 errors (e.g., the position of the transducers, the picking, the sampling rate of the oscilloscope
32 ($2 \mu\text{s}$) and the length of the samples), the velocity measurement uncertainty is about ± 55 m/s
33 for P-waves and ± 10 m/s for S-waves.

34 3D images (photogrammetry)

35 Based on photogrammetry techniques, 3D images of the different samples have been done. We
36 then, obtained their orthomosaic (i.e. a projection in the plane along an axis of the 3D object
37 without distortion). The photogrammetry technique consists in reconstructing a 3D image of an
38 object from several photographs taken from different complementing view points by
39 stereoscopy. The camera is a SONY A7-RIV apparatus with a resolution of 61 M pixels and a
40 fixed 35 mm lens. The photogrammetry processing was performed thanks to the Agisoft
41 Metashape Pro® software. The processing consisted in following a predefined workflow which
42 begins with the repositioning of the 2D images by comparing some remarkable points or tie
43 points. Then, a dense cloud of point was built from which the 3D image of the sample is
44 reconstructed. Finally, the 3D textured images were projected onto a cylindrical surface aligned

1 on the core geometries to unwrap their borders into a flat image. From these orthoimages and
2 3D images, a naked eye macroscopic description was made (Figure 3).

3 3 RESULTS

4 The average uncertainties/errors related to the measurements are recalled as: $\pm 0.5\%$ for the
5 effective porosity, $\pm 25 \text{ kg/m}^3$ for the bulk density/grain density, $\pm 0.02 \text{ mD}$ for the permeability
6 and ± 55 and 30 m/s for the P- and S-wave velocities respectively. Finally, the depth uncertainty
7 is $\pm 0.35 \text{ m}$ for the facies A, $\pm 0.65 \text{ m}$ for the facies B, $\pm 0.70 \text{ m}$ for the facies C and $\pm 0.25 \text{ m}$
8 for the facies C'.

9 3.1 Macroscopic description

10 Figure 3 shows the orthoimages obtained from the 3D images of four 4 cm-diameter samples
11 (one per facies). We consider each presented sample as representative of its corresponding
12 facies.

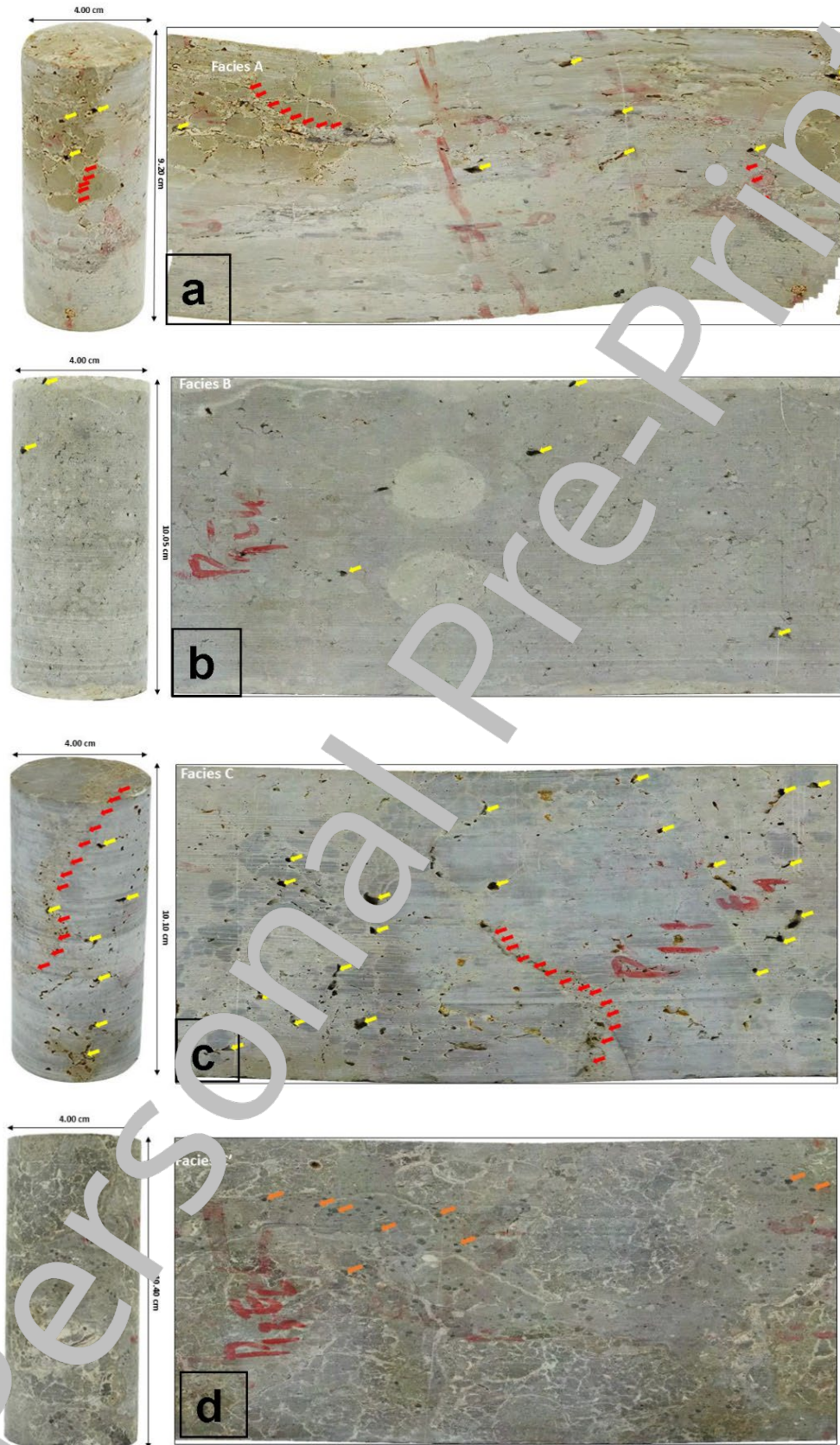
13 All these samples are made of limestone matrices and clasts which are essentially composed of
14 low-Mg calcite mineral. A low proportion of detrital mineral such as quartz, phyllosilicates
15 (palygorskite, kaolinite, illite, smectite) and iron oxides (goethite) are also present (Ménillet &
16 Edwards, 2000; Aldana et al., 2021). These samples can be classified as either micritic
17 limestones according to Folk (1959) or mudstones/wackestones according to Dunham (1962)
18 and may correspond to the carbonates lithofacies defined by Trautmann (1974). For our
19 samples, beyond the rock fabrics, it is rather the diagenetic elements caused by the weathering
20 in the VZ and/or the minor tectonic events which make it possible to differentiate or
21 discriminate our petrophysical facies or (electrofacies). The alteration/weathering results in the
22 presence of dissolution vugs ($< 5 \text{ mm}$) and some mineralogical transformations (Aldana et al.,
23 2021), whereas the fractures ($>> 1 \text{ mm}$), cracks ($> 1 \text{ mm}$) and microcracks (about $15 \mu\text{m}$) origin
24 remains unknown as they are either linked to tectonics or mechanical weathering (Lorain,
25 1973; Trautmann, 1974).

26 Facies A

27 We can see in Figure 3a that samples of facies A, located between 7.80 and 8.50 m deep, are
28 characterized by a rather uniform micritic texture of beige to yellowish color. It may correspond
29 to the compact and fine-grained limestones defined by Trautmann (1974). Moreover, it is quite
30 easy to distinguish cracks (red arrows) and open cavities (yellow arrows). These structures may
31 be related to weathering and tectonics phenomena. These cracks appear to be filled with a
32 different material based on the change of color, which could result from recrystallization of new
33 minerals different from the matrix ones. These minerals may be diagenetic silica or
34 phyllosilicates highlighted by Aldana et al (2021). Regarding the vugs, one may note the
35 presence of reddish color inside, characteristic of iron oxides. Finally, the cracks seem to be
36 penetrative and therefore potentially connected.

37 Facies B

38 Facies B (Figure 3b) is defined as less consolidated on well logs (Figure 2). However, it appears
39 that the taken samples, located between 11.80 and 13.10 m deep, are rather
40 consolidated/lithified with a uniform and homogeneous matrix covering the whole samples.
41 The color is greyish and differs from facies A color. The facies B may correspond to the
42 biogenic facies or a monogenic brecciated limestone. We find in this matrix, white or light
43 grey angular clasts which may have a biological origin. There are few vugs highlighted with
44 yellow arrows. They are lower in number compared to those of samples of facies A. The
45 presence of cracks is almost non-visible on this facies.



1
2 Figure 3. 3D images (left) and orthoimages (right) of a 4 cm-diameter samples for from a to d:
3 facies A, B, C and C'. Red arrows highlight the fractures and cracks, yellow arrows highlight
4 the dissolution vugs and orange arrows highlight the black inclusions.

1 Facies C

2 Located between 14.50 and 15.90 m deep, samples of facies C (Figure 3c) are also characterized
3 by a micritic texture and seems to be much more altered and fractured than the other facies
4 when considering the number and size of vugs and fractures/fissures. We can observe first
5 matrix of grayish color, as for facies B, which is replaced in some places by another matrix of
6 lighter color. This later matrix is more sensitive to the alteration. The presence of two matrices
7 suggests a polygenic brecciated limestone corresponding to two episodes of sedimentation. As
8 for the facies A, it is easy to note the presence of fractures and cracks (red arrows), and vugs
9 (yellow arrows) of all sizes. Within the fractures, we find the light matrix which seems to be
10 less compacted and more affected by cavities than the grey matrix. On this sample, the fracture
11 highlighted in red crosses the entire volume.

12 Facies C'

13 Finally, samples of facies C' (Figure 3d), located between 17.0 and 17.50 m deep, are slightly
14 different from the other facies in terms of color as it is a mosaic of different variations (grey,
15 light grey, beige). The samples are characterized by a very well consolidated matrix with a
16 micritic texture in which we see angular to sub-angular clasts (0.5 to 3 mm of diameter). They
17 are limestone fragments of diverse origins trapped in a matrix which may suggest a polygenic
18 brecciated limestone in terms of lithofacies. Other circular clasts of a dark/black color and small
19 in size (highlighted in orange on the figure) are presents with a probable organic origin may
20 suggest ooids/oncoids. The fragmented clasts are sometime surrounded by a beige colored film
21 corresponding to biological or microbiological constructions or a late sedimentation of a second
22 matrix. We also find this film in a more diffuse and extended shape forming rings in some
23 places. Finally, this facies is almost devoid of pores and visible cracks at this scale of
24 observations.

25 Regarding the discussion ahead and from a purely petrophysical point of view, fractures, cracks
26 and dissolution vugs will be referred to as macroporosity while the microporosity will refer to
27 microcracks and micropores inside the micritic matrices.

28 3.2 Reservoir properties of the Braze Limestone

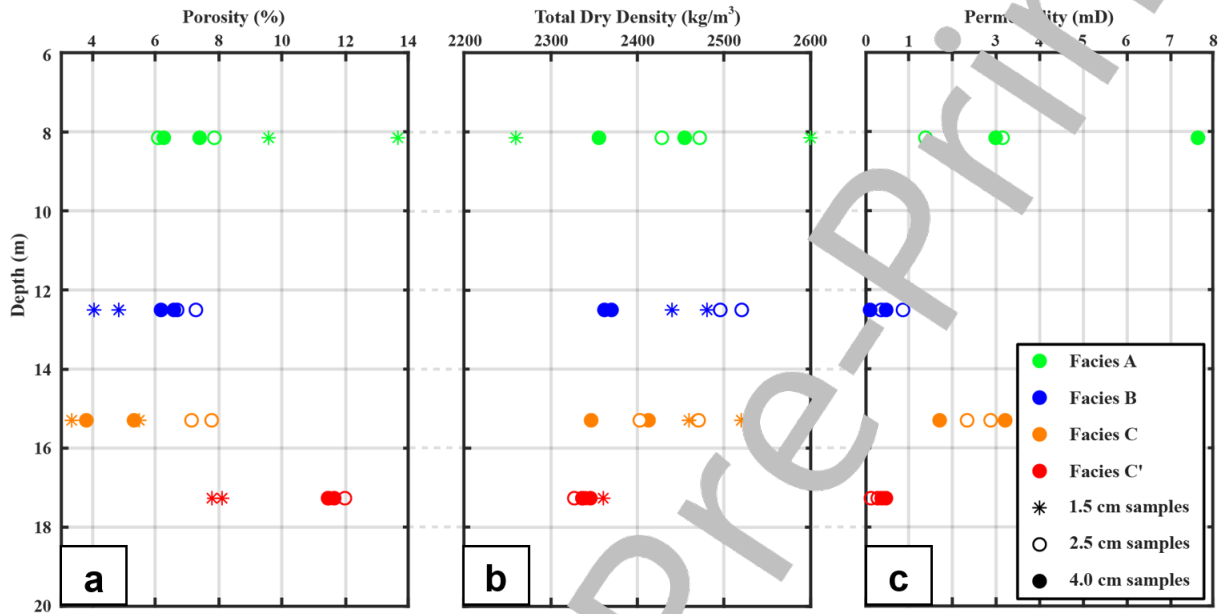
29 Effective porosity, bulk density and permeability

30 As seen on Figure 4a, the effective porosity of 2.5 and 4 cm diameter samples ranges between
31 3.83 to 11.96 %, with an average value of 7.81 %. There is no clear trend with depth for the
32 three first facies A, B and C as we have close average values. The facies C has the lowest
33 average effective porosity of 6.04 %, with a dispersion of 1.53% while facies C' stands out as
34 the most porous one with a value of 11.67% in average and a dispersion of 0.18%. We note a
35 small porosity variation between the samples of 2.5 cm diameter and 4.0 cm diameter. Indeed,
36 the average porosity of the 2.5 cm samples is more important than the average porosity of the
37 4 cm samples (8.07% for the 2.5 cm samples and 7.36% for the 4 cm). This variation is more
38 pronounced for facies C where the samples of 4.0 cm and 2.5 cm diameter have an average
39 porosity of 4.6 % and 7.45%, respectively.

40 For the 2.5 and 4 cm diameter samples, the dry bulk density (Figure 4b) ranges between 2326
41 and 2520 kg/m³. As for the effective porosity, no specific trend is found with depth. However,
42 facies C' has a lower dry bulk density than the other facies. A variation of the dry bulk density
43 with sample size is observed for facies C and B.

44 The intrinsic permeability, presented on Figure 4c, is globally low and ranges between 0.08 and
45 7.66 mD. Facies B and C' have the two lowest average permeabilities of 0.43 and 0.29 mD

1 respectively. The dispersion in their permeability values is also very low compared to the others.
 2 In contrast, the facies A and C have the highest average permeabilities (3.66 and 2.53 mD,
 3 respectively) and the strongest dispersion, especially for facies A. Regarding the size, there is
 4 a clear difference of average permeability as the 2.5 cm samples have a lower permeability in
 5 average than the 4 cm samples (1.40 against 2.10 mD, respectively).



6
 7 Figure 4. Variations with depth of the measured effective porosity (a), dry bulk density (b) and
 8 absolute permeability (c) for the different facies.

9

10 Mercury (Hg) porosity, bulk density and pore size

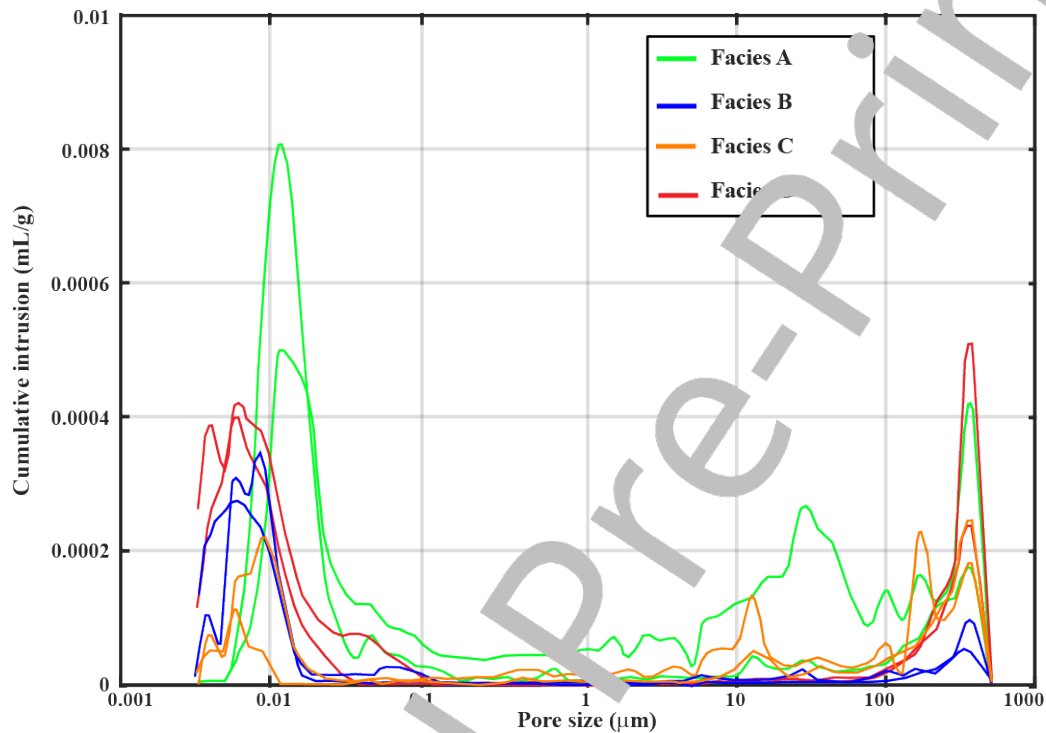
11 Porosity and dry bulk density obtained with Hg-injection are plotted in Figure 4A and B with
 12 stars.

13 The porosity accessible to mercury varies from 4.02 to 13.61% and the dry bulk density varies
 14 from 2260 to 2520 kg/m³. In terms of order of magnitude, these ranges are similar to the
 15 previously obtained ones. However, there are some differences between the facies. Indeed, the
 16 Hg-porosity of facies A show a higher value and dispersion. For facies B, C, and C' Hg-porosity
 17 is lower than the effective porosity. This is more pronounced for facies C'.

18 The Hg-dry bulk density seems to be in a better agreement with the water saturation method. It
 19 is also the case of the grain density (in average) for both measurement. Indeed, adding the
 20 mercury bulk density values doesn't change the global trend, neither the average value for each
 21 facies. We may notice that the dispersion of facies A bulk density is, as for the porosity, largely
 22 increased with the mercury measurement. Finally, facies C and C' dry bulk density are slightly
 23 increased by this measurement, especially for facies C while facies C' keeps its strong
 24 homogeneity.

25 From a theoretical point of view, it is expected to have a good agreement between mercury
 26 porosity and hydrostatic weighing dry bulk density as the latter is not affected by the non-
 27 wetting property of Hg. However, it is not the case for the porosity as Hg-porosity is computed
 28 based on both bulk density and grain density. We note that the grain density values are almost
 29 systematically underestimated in the case of mercury injection method. The latter is less
 30 accurate than hydrostatic weighing method (if pore vacuum has been made correctly) because

1 of the limits of the accessibility of mercury. Indeed, we cannot access pores below 4 nm,
 2 especially clay materials (Leroy et al., 2019). Moreover, the Beauce limestones structure,
 3 showing localised large pores and fractures, create an obvious size effect that strongly affect
 4 the porosity more than the dry bulk density.



5
 6 Figure 5. Pore size distribution obtained from mercury measurement of the 8 (2 samples per
 7 facies) smallest samples.

8
 9 The Hg measurement gives access to other reservoir properties which are the pore size
 10 distribution and the average pore diameter (with respect to the previous cited limitations). We
 11 can see that the pore size distribution (Figure 5) are quite uniform from one facies to another,
 12 although not of the same amplitude. All facies mainly present two peaks: the first one around
 13 0.003 to 0.01 μm and the second one around 100 to 300 μm and above. There are in addition
 14 few specific variations with some additional small peaks (for example, at 30 μm for one sample
 15 of facies A and at 1 μm for facies C). Considering the limits of the Hg injection method, the
 16 peaks around 300 μm and more can be considered as not representative of our pore space.
 17 Indeed, these peaks correspond to the surface conformance effects observed at very low
 18 pressure caused by the presence of macropores or vugs on the edge of the sample (Zinszner &
 19 Pellerin, 2007).

20 Regarding the average pore diameter, we noticed that facies A and C have the largest average
 21 pore diameters, while B and C' have the smallest ones. From this average pore diameter, it is
 22 obvious that mainly the microporosity (porosity found in the matrices) of the different samples
 23 has been assessed by the Hg injection method and only a small porportion of the macropores
 24 has been integrated.

25 3.3 Elastic properties of the Beauce limestones

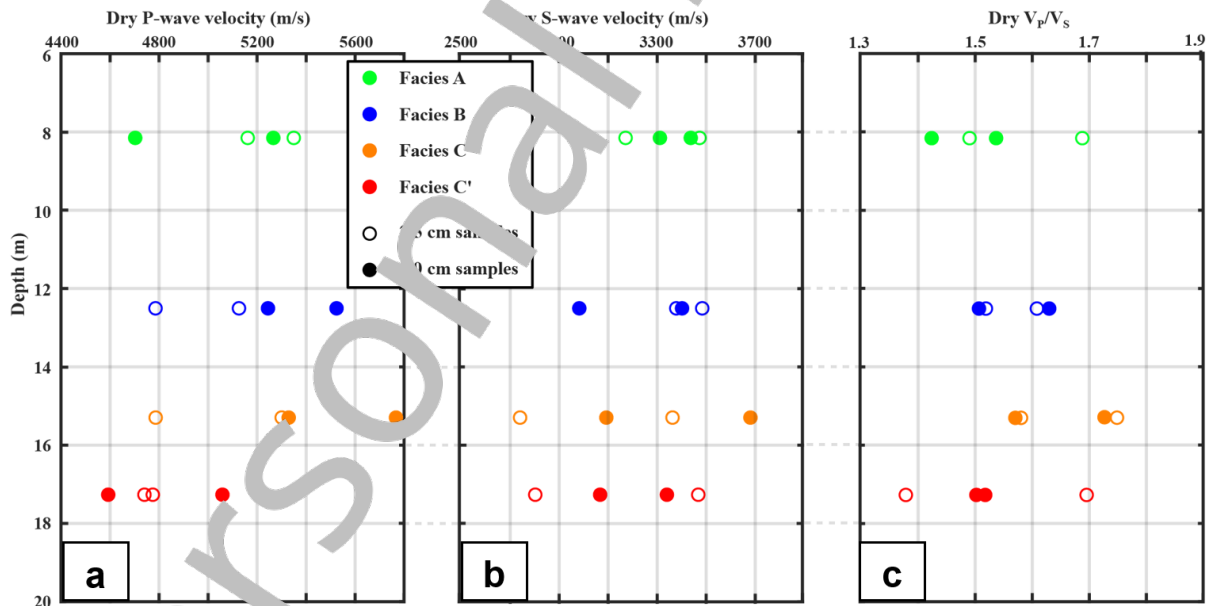
26 The acoustic measurements allow us to obtain P- and S-wave velocities of the different samples.
 27 They are plotted as function of depth in dry and saturated condition in Figure 6 and Figure 7,

1 respectively. As for the petrophysical properties there are no clear tendency regarding the depth
2 and dispersion between the samples are important and even more depending on the facies.

3 A detailed analysis shows that facies C' has the lowest P- and S-wave velocities both in dry and
4 water saturated conditions with the lowest dispersion, especially for P-waves. Indeed, the other
5 facies are much more disperse, especially the facies C with P- and S-wave dry velocities varying
6 from 4800 to 5800 m/s and 2750 to 3700 m/s, respectively. This facies C is also characterized
7 by the highest P- and S-wave velocities in average, although it must be considered with caution
8 in the view of the huge dispersion.

9 Facies A and B have very similar P-wave velocities in average both in dry and water saturated
10 conditions, with similar dispersion for both. The difference is more pronounced in S-wave
11 velocities, especially in dry conditions where we have 3110 m/s for facies A against 3308 m/s
12 for facies B. We can note that the dispersion in saturated conditions is the lowest for the P-
13 waves of facies B. Regarding the ratio V_p/V_s , the values are globally higher in saturated
14 conditions than in dry ones. Facies A and B have similar average values in both conditions,
15 whereas the facies C and C' are close in saturated conditions (1.60 and 1.58 respectively). The
16 dispersion is globally high for all facies both in dry and saturated conditions. We note that our
17 V_p/V_s ratio is globally in good agreement with several studies made on carbonate reservoirs
18 (Rafavich et al., 1984; Anselmetti & Eberli, 1993; Al-Jeifri et al., 2003) showing a V_p/V_s ratio
19 values between 1.6 to 2.2. However, these are much deeper reservoirs at higher pressures and
20 therefore certainly more compact and rigid than our samples.

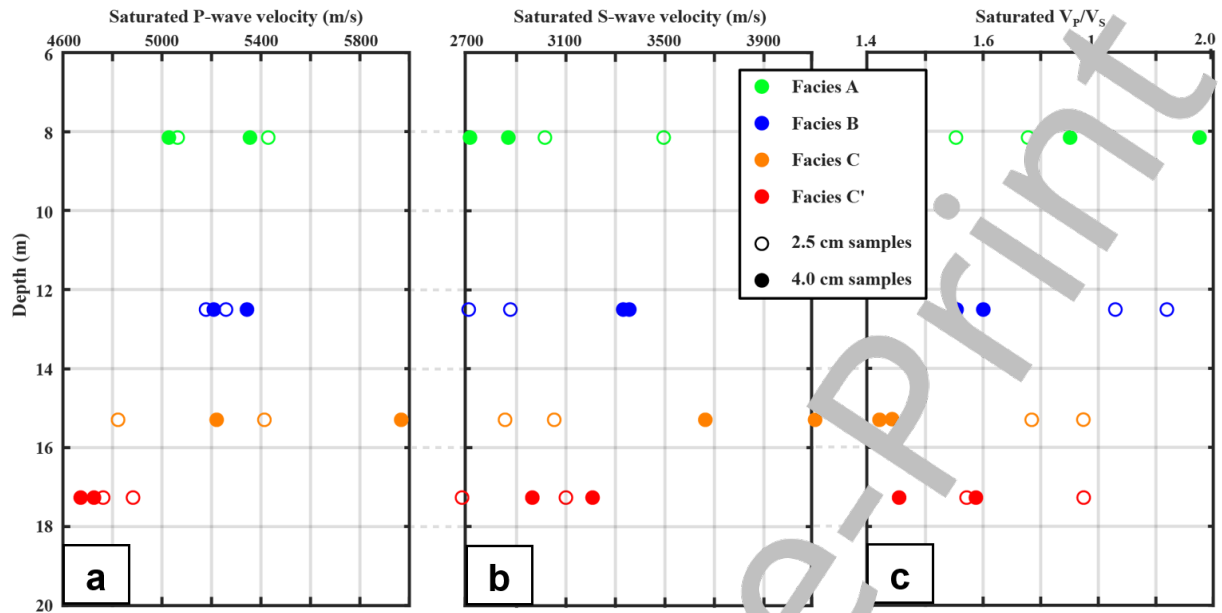
21



22

23 Figure 6. Variation with depth of the Dry P-waves velocities (a), S-waves velocities (b) and
24 V_p/V_s ratio (c).

25



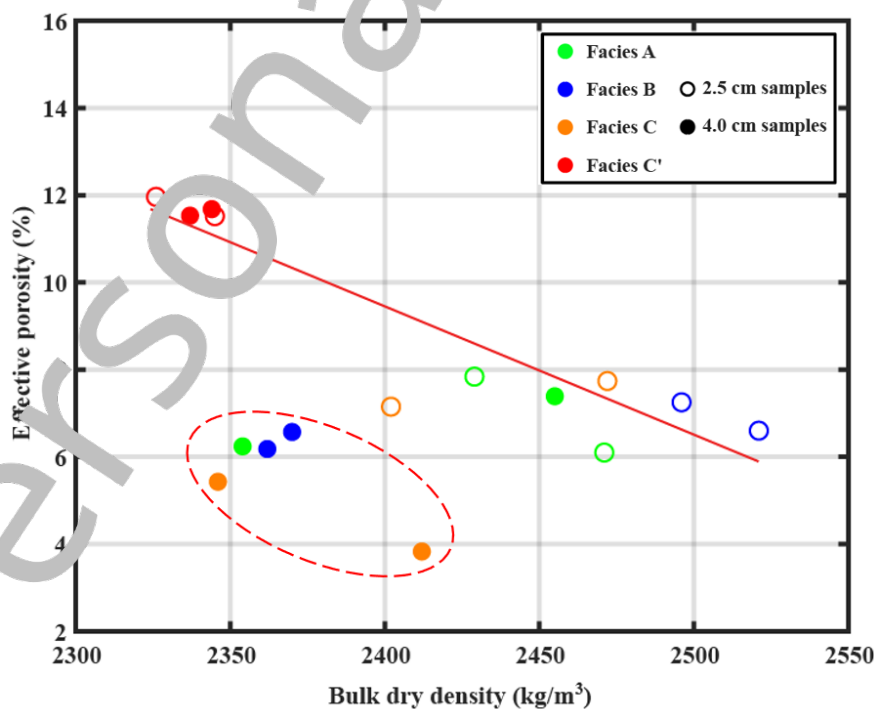
1
2 Figure 7. Variations with depth of the saturated P-waves velocities (a), S-waves velocities (b)
3 and V_p/V_s ratio (c).

4

5 4. DISCUSSION

6 4.1 Effective porosity-bulk density relationship: method limitations

7 It is expected, at constant mineralogy, that an increase of total porosity linearly leads to a
8 decrease of bulk density. This is not the case for our samples as we can see on Figure 8.



9

10 Figure 8. Petrophysical relations between effective porosity and dry bulk density. Red line:
11 regression line without the five samples in the dashed red ellipsoid with the following
12 corresponding equation: $\varphi_{\text{eff}} = -0.0386 \rho_{\text{b_dry}} + 105.71$ and $R^2=0.84$.

1 A variation in the sample mineralogical composition (presence of other minerals than calcite),
2 could explain this out-trend of some samples. This is well correlated with the grain density that
3 is not the same as pure calcite density (2710 kg/m^3). Only, facies C' samples are the closest to
4 pure calcite with an average grain density of 2647 kg/m^3 . It is also in good agreement with the
5 study of Aldana et al (2021) showing that the consolidated part of the Beauca Limestone is
6 composed by almost 90% of calcite and the remaining is made of quartz and clay. However,
7 this mineralogical composition should still lead to a good linear relationship and this slight
8 variation (from 100% of calcite) is not enough to explain the large deviation of some samples.
9 This indicates that the mineralogical aspect is not the only factor affecting the porosity results.
10 The method limitation and the sample size could affect the effective porosity measurements
11 and explain this result.

12 Considering effective porosity, the samples can be divided into two clusters. On one side, facies
13 C' appearing as homogeneous both in terms of pore structure (Figure 4) and grain density. This
14 results in a relatively better linear relationship (although not exact with $R^2=0.68$) for this facies.
15 On the other side, only facies A follows the expected linear trend when 3 samples are considered
16 instead of 4 samples. The out-trend samples (a 4 cm diameter sample) has probably a low
17 effective porosity, related in some way to the sample size (total volume). Indeed, we saw
18 (Figure 8) a clear segregation between the two types of samples (2.5 and 4 cm diameters) which
19 is more pronounced for the facies B and C. Furthermore, this segregation is highlighted also by
20 the grain density as an average, the 2.5 cm diameter samples have a grain density of 2652 kg/m^3
21 whereas the 4 cm diameter samples have a grain density of 2563 kg/m^3 . Our interpretation
22 behind these observations is that, the presence of vugs and fractures leads to an underestimation
23 of samples effective porosity and then grain density. Moreover, this underestimation is
24 exacerbated by size effect as large samples incorporate more vugs, fractures or weathered
25 minerals (with lower density minerals replacing the calcite mineral) than smaller ones. Thus,
26 there may be a measurement bias or limit of the hydrostatic weighing method due to vugs,
27 fractures or dead (disconnected) pores not observed with this method. The method may
28 encounter problems when dealing with weathered and/or fractured samples with large vugs or
29 fractures which can make the saturated or immersed weight measurements more challenging
30 (Amyx et al., 1960; API, 1996). However, efforts (repeating saturation and weighting step)
31 have been made to mitigate these problems. Finally, by removing the five encircled samples
32 (causing the deviation), we find a good correlation between effective porosity and dry bulk
33 density, materialized by the red line ($R^2=0.84$) for the remaining samples.

34 **4.2 Permeability-porosity relationships and pore size effect**

35 Figure 9a shows permeability with respect to the effective porosity. We first saw a really poor
36 correlation between logarithm of the permeability and effective porosity with a similar
37 clustering effect as seen previously (A-B-C on one side and C' on the other). This is not
38 surprising because these types of relationships are often linear for homogeneous reservoirs like
39 silico-clastic reservoirs (Berg, 1970; Nelson, 1994). For carbonate reservoirs, the effective
40 porosity control on permeability is more questionable. Other factors like texture, pore size, pore
41 connectivity, or tortuosity may have a greater influence (Lucia, 1995, 2007; Bernabé &
42 Mameu, 2015; Cardona & Santamarina, 2020; Bohnsack et al., 2020; Rembert et al., 2023).

43 This absence of correlation is highlighted by facies C' which shows the highest porosity but the
44 lowest permeability. To assess this, it is necessary to consider the structure and microstructure
45 of the pore space (connectivity, geometry, tortuosity) which can be approached by the pore size
46 (average pore size) obtained from the mercury injection method (Figure 5). Thus, considering
47 an average pore diameter by facies, we compute a predicted permeability based on the Kozeny-
48 Carman (KC) relationship (Carman, 1997; Zinszner & Pellerin, 2007):

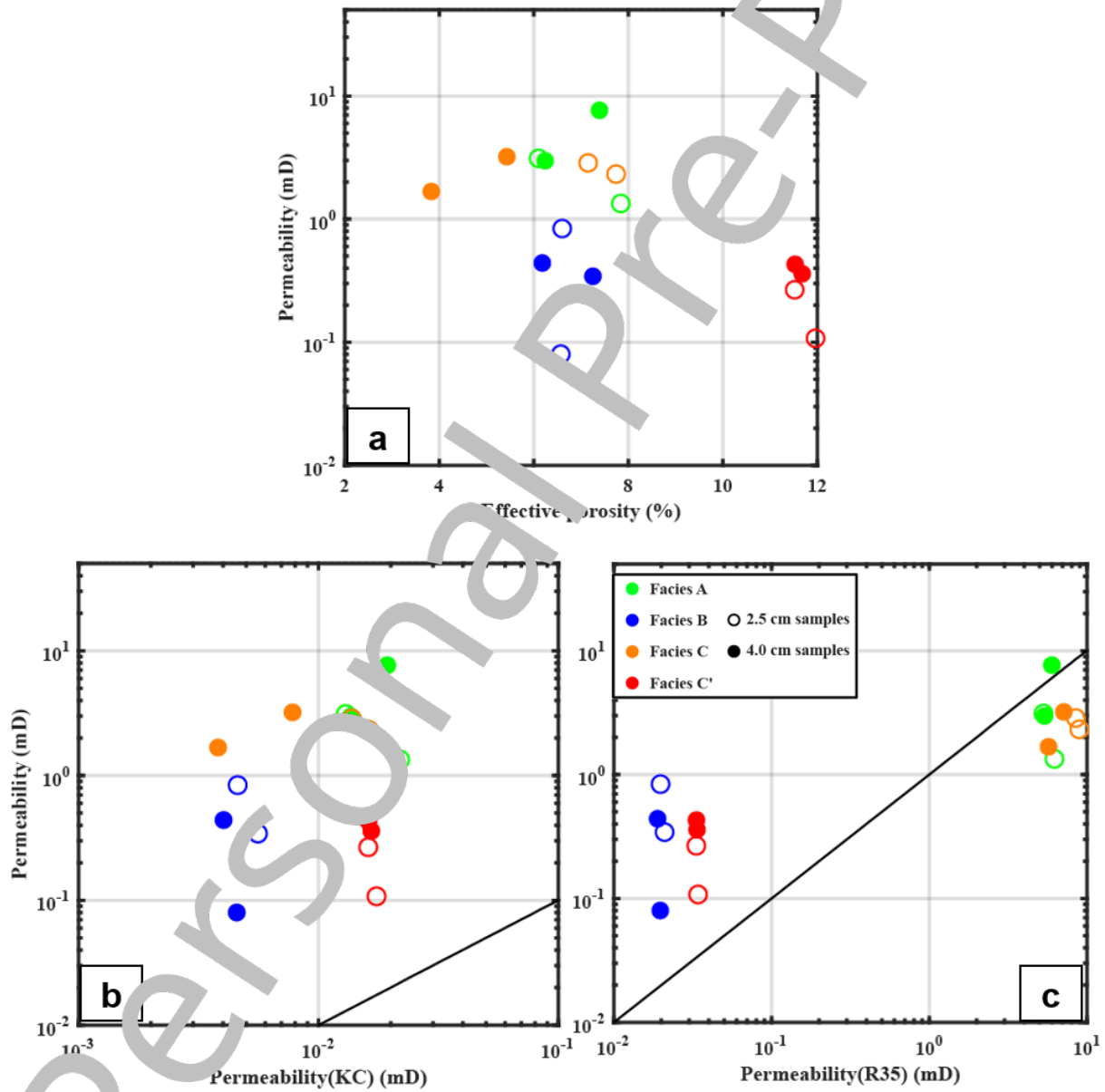
$$k = \frac{\varphi^3}{2S_{gr}^2(1 - \varphi)^2}, \quad (4.1)$$

where S_{gr} is the specific surface area per unit of grain (μm^{-1}) and is equal to $\frac{2\varphi}{r(1-\varphi)}$, φ being the porosity (%) and r being the pore radius (μm).

We compared it to, a very used empirical permeability model for carbonate reservoirs, integrating also the pore size information, known as Winland model (Kolodziej, 1980).

$$\log(r_{35}) = 0.723 + 0.588 \log(k_{air}) - 0.864 \log(\varphi), \quad (4.2)$$

where k_{air} is the air permeability (mD), and r_{35} is the pore radius at 35% saturation of mercury injection.



9
10 Figure 9. a) Measured permeability versus effective porosity. b) Measured permeability versus
11 Kozeny-Carman (KC) predicted permeability. c) Measured permeability versus Winland (R35)
12 empirical permeability. Black line: 1:1 line.

1 Winland predicted permeabilities are globally better than the KC ones. Permeabilities obtained
2 by KC model (Figure 9b) always underestimate (sometimes by two orders of magnitude) the
3 measured ones, while the permeabilities obtained by Winland model (Figure 9c) are globally
4 in the same order of magnitude than the measured ones. Although KC model fails to well predict
5 the measured permeabilities, it explains to a lesser extent the influence of microporosity and
6 macroporosity on permeability. Indeed, facies B and C' characterized by very small pore
7 diameters and a more homogeneous effective porosity (which could suggest a more
8 homogeneous pore structure) show pertinent prediction (same order of magnitude) of
9 permeabilities than for facies A and C. The latter are more heterogeneous (more macropores)
10 in terms of pore structure, therefore more difficult to model by the KC model. Thus, for facies
11 B and especially facies C', the microporosity found in the matrices, essentially controls the
12 permeability. In the case of an homogeneous facies with mainly microporosity as these two
13 facies, they can be modelled as reservoirs with an intergranular/intercrystalline porosity (Lucia,
14 1983; Ehrenberg & Nadeau, 2005; Baechle et al., 2008).

15 The Winland predicted permeabilities show a clear segregation related to the structure or
16 microstructure of the different facies with facies B and C' on one side, and A and C on the
17 other. The latter are less recovered by the KC model but well estimated by the Winland model.
18 A slight overestimation is observed and may be due to the uncorrected air permeability used in
19 the Winland model. In addition, other studies have shown that the mercury injection saturation
20 to be considered for the choice of pore radius can vary depending on the structure of carbonates
21 reservoirs (e.g.: 25% of saturation for Pitman (1972) ; 15% for Jaya et al., (2005) ; 50% for
22 Rezaee et al., (2006) and 20% for Miaomiao et al. (2022)).

23 We highlight here, that the permeability-porosity relationship of our carbonates is very
24 dependent on the microporosity which is mainly linked to the micritic matrices of our rocks and
25 the macroporosity due to weathering and fracturation. This micritic texture controls the
26 microporosity therefore the effective porosity. We have also a great influence of the
27 macroporosity controlled by the presence of fractures, cracks and vugs which probably connects
28 the microporosity as shown by the presence of iron oxides and phyllosilicates near those
29 macropores. Therefore, the presence of macropores increases the permeability without
30 increasing the overall effective porosity as shown by Lucia (1983).

31 We can summarize these observations with on one side, microporous and homogeneous
32 samples for which permeability is controlled by the microporosity and can be correctly
33 approached by KC-model. On the other side, heterogeneous samples are more difficult to
34 describe, but their permeability order of magnitude can be correctly recovered by Winland
35 model with strong limitations as the heterogeneities growth.

36 4.3 Acoustic properties analysis

37 V_P , V_S relationship and pore fluid effect

38 Crossing saturated velocities and their ratio (Figure 10) shows no clear linear correlation
39 between P - and S -wave velocities. On Figure 10a, the regression (best fit) leads to a $R^2=0.5$ (not
40 shown in the figure). On Figure 10b, no clear relation is found (best fit with $R^2=0.01$, not shown
41 in the figure) with again five samples which exhibit relatively low V_P/V_S ratio. Once these
42 samples are removed, the correlation improves but is still low ($R^2=0.59$, red line). This difficulty
43 to directly link V_P to V_S is interpreted in terms of heterogeneity (macropores and mineralogical
44 variation) characterizing the Beauce Limestones. It is highlighted also by the empirical models
45 of Castagna & Backus (1993) :

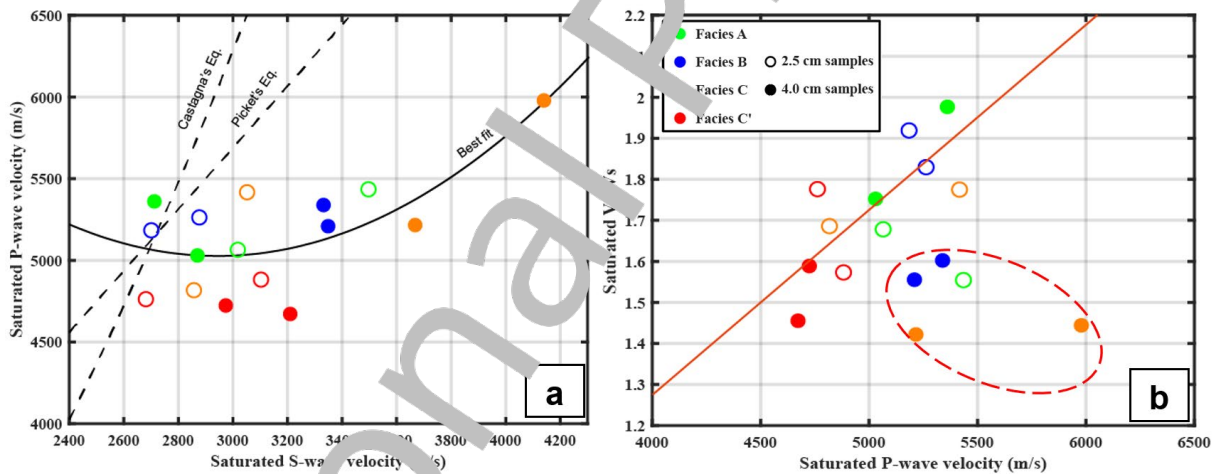
$$46 \quad V_S = -0.055V_P^2 + 1.017V_P - 1.031, \quad (4.3)$$

1 and Pickett (1963) :

2
$$V_S = \frac{V_P}{1.9},$$

3 with V_S and V_P in km/s.

4 Indeed, these two models significantly underestimate, the S-wave velocities regardless of the
 5 facies and overestimate P-wave velocities, even though the Pickett's (Root Mean Square Error:
 6 RMSE=27) is slightly better than the Castagna's one (RMSE=31). The mineralogical variation
 7 (due in particular to the alteration in the vadose zone) present in some samples could partly
 8 explain this difference. Indeed, the empirical models are based on a monomineral (pure calcite)
 9 composition which we saw, is not our case. Moreover, the presence of fractures/fissures and
 10 vugs on certain samples influences the rigidity of these samples, which causes low V_P values,
 11 which results in lower values of the V_P/V_S ratio for certain samples. The five encircled samples
 12 (Figure 10b) show high V_S values with respect to V_P explaining the low V_P/V_S ratio values.
 13 This observation shows that the mineralogy and the macroporosity have more impact on V_P
 14 than V_S . Indeed, these samples have the lowest grain densities and are more affected by
 15 macropores in particular facies A and C (Figure 3). This may be linked to the increased
 16 weathering and fracturing undergone by facies A, B and C unlike facies C', located in the
 17 phreatic zone, so more preserved and devoid of macropores.



18

19 Figure 10. a) Saturated V_P versus Saturated V_S . Dashed lines: empirical model of Castagna &
 20 Backus (1993) and Pickett (1963). Black line: best fit line of the plotted data with the equation:
 21 $V_P = 0.0007V_S^2 - 1.8778V_S + 10729$. b) Saturated V_P/V_S versus saturated V_P . Red line:
 22 regression line of the plotted data without the five encircled samples leading to the following
 23 equation: $V_P/V_S = 0.0004V_P - 0.5097$ and $R^2= 0.59$.

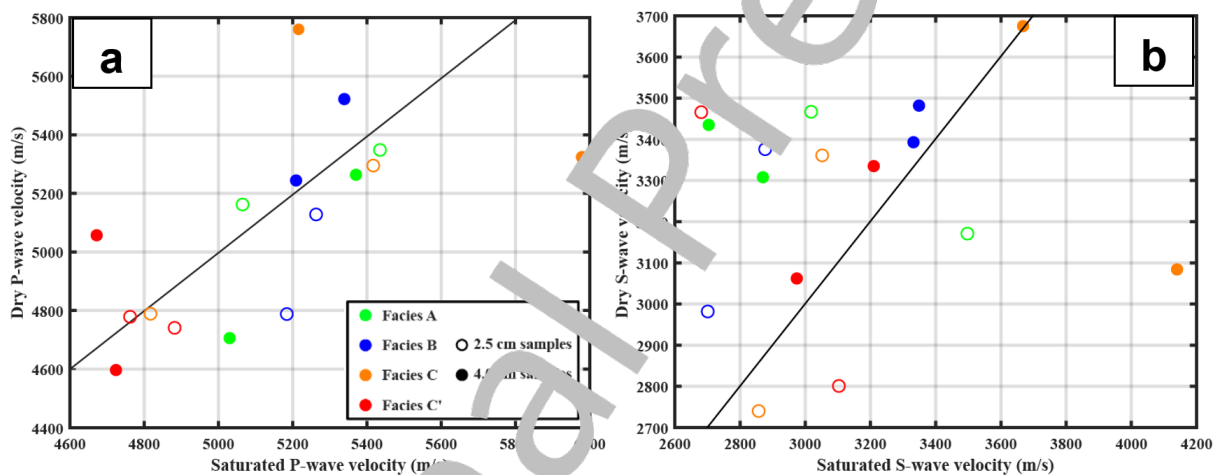
24

25 **Pore fluid effect**

26 Figure 11 shows the comparison between dry and water saturated V_P and V_S velocities. We see
 27 a relatively better linear correlation for V_P than for V_S . Moreover, saturation tends to
 28 homogenize V_P but not V_S . This homogenization of the P-wave velocities is in particular more
 29 visible for facies B and C'. In addition to this homogenization, saturation has the effect of
 30 increasing P-wave velocities. This is consistent with several studies carried out on both silico-
 31 clastic and carbonates reservoirs (Cadoret et al., 1995; Domenico, 1976; Assefa et al., 2003;
 32 Lebedev et al., 2009). This effect is also consistent with the theory (Gassmann, 1951; Biot,

1 1956). Indeed, saturation tends to increase the effective pressure by increasing the pore
 2 pressure, which has the effect of increasing the stiffness of the rock and therefore increases the
 3 bulk modulus. This phenomenon was observed on carbonates by Cadoret et al. (1995) who
 4 suggest a competition between the stiffness effect observed at high saturation and the softening
 5 effect at low saturation which is characterized by an increase of the bulk density and therefore
 6 a decrease of V_P . Thus, depending on the saturation pattern (which itself depends on the pore
 7 structure, pore connectivity, especially non-connected pores) saturated V_P may not be always
 8 higher than dry V_P . Regarding V_S , the saturation is only manifested by a decrease in the
 9 velocities which is also consistent with the theory. According to the theory (Gasparmann, 1951;
 10 Biot, 1956), a change of fluid has no effect on the shear modulus of the rock (shear modulus
 11 equals to zero for fluids). However, Verwer et al. (2008) shows that the shear modulus in
 12 limestones can be sensitive to saturation and this variation may even be related to rock texture.

13 So, for complex reservoirs as the Beauce limestones, the behavior of the P- and S-wave
 14 velocities as function of the water saturation is very complex and therefore may depend on the
 15 porosity, the pore structure, the texture, the saturation pattern and even the frequency which
 16 could explain why in our case few samples do not follow the general trend.



17
 18 Figure 11. Comparison between dry and saturated velocities for V_P (a) and V_S (b). The black
 19 lines correspond to the 1:1 line.

20

21 4.4 Controlling factors on geoelectric and geoelectromagnetic properties of Beauce Limestones

22 Effective porosity and pore structure effect

23 Porosity is the first controlling factor of the elastic properties of sedimentary rocks (Wyllie et
 24 al., 1956; Pickens, 1963; Gardner et al., 1974). However, Anselmetti & Eberli (1993) have
 25 shown the role played by the pore structure in the dispersion of the acoustic velocities for a
 26 given porosity in carbonate reservoirs. Indeed, carbonate reservoirs have a very complex pore
 27 structure (Chouque & Pray, 1970; Lucia, 1995; Lønøy, 2006) making velocity-porosity
 28 relationship less predictable.

29 On Figure 12a, we note a decrease in V_P when the porosity increases that is consistent with
 30 several works on carbonates (Rafavich et al., 1984; Wang et al., 1991; Anselmetti & Eberli,
 31 1993; Palaz & Marfurt, 1997; Assefa et al., 2003; Baechle et al., 2008; Regnet et al., 2019). On
 32 Figure 12b, we notice a very poor relationship between V_P/V_S and the effective porosity,
 33 imputable probably to S-wave velocities (much more scatter). The control of the effective

1 porosity over V_s is less effective, resulting in low values of the V_p/V_s ratio of some samples.
 2 Moreover, as in the previous relationships removing these samples, leads to a better trend where
 3 a decrease in the ratio produces an increase in effective porosity, consistent with some works
 4 for low porosity carbonates (<15%) (Tatham, 1982; Rafavich et al., 1984; Assefa et al., 2002).

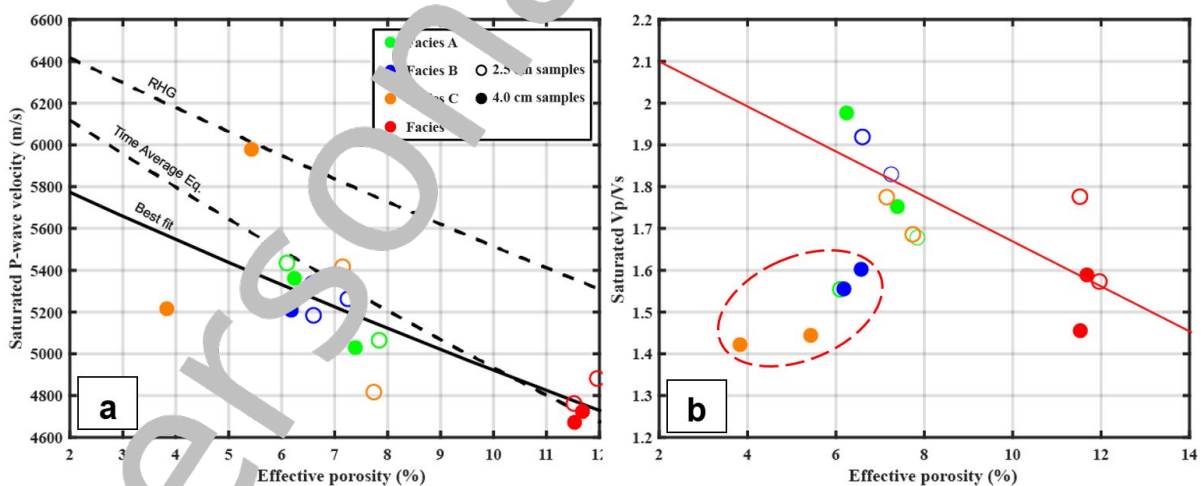
5 To infer porosity from P-wave velocities, the WTA (Willie Time Average) and RHG (Raymer-
 6 Hunt-Gardner) empirical models are used (Mavko et al., 1998). The WTA relation (equation
 7 4.5) is a heuristic relation and considers that the transit time (inverse of the velocity) of a rock
 8 is the sum of the transit times of each constituent. The RHG relation (equation 4.6) is a
 9 modification of the WTA relation, intended for low porosity values. These relations are written
 10 as:

$$11 \quad \frac{1}{V_p} = \frac{\phi}{V_{Pf}} + \frac{1-\phi}{V_{Pm}}, \quad (4.5)$$

$$12 \quad V_p = (1-\phi)^2 V_{Pm} + \phi V_{Pf}, \quad (4.6)$$

13 where V_{Pf} (m/s) and V_{Pm} (m/s) are the P-wave velocity of the fluid (water) and the matrix
 14 (calcite). For these relations, the acoustic properties of the matrix are those of pure calcite with
 15 V_p and V_s equivalent to 6640 and 3440 m/s respectively according to Markov et al. (1998).

16 The RHG relationship overestimates (about 11% on average, RSME=142) quite significantly
 17 the velocities obtained while the WTA relation only overestimates them slightly (about 4% on
 18 average, RSME=27) with some discrepancies depending on the facies (Figure 12a). Two factors
 19 can explain this overestimation, starting with the use of a unique and homogeneous mineralogy
 20 for the two models, which is, again, not the case for our samples. Then, these two models are
 21 suitable for rocks under high effective pressure (compact and stiff rocks) which minimizes the
 22 effect of cracks and microcracks resulting in higher velocities (Mavko et al., 1998). Thus, our
 23 samples located in the vadose zone are characterized by the presence of these microcracks,
 24 cracks and vugs which tend to lower the velocity as shown by Anselmetti & Eberli (1993) and
 25 Panza et al. (2019).



26
 27 Figure 12. a) Effect of the effective porosity on saturated V_p and two empirical petroacoustic
 28 models (dashed lines for WTA and RHG empirical models). Bold line: best fit line of the plotted
 29 data with the equation: $V_p = 6009.3e^{-0.02\phi_{eff}}$ and $R^2 = 0.60$. b) Saturated V_p/V_s versus effective
 30 porosity. Red line: regression line of the plotted data without the five encircled samples with
 31 the following equation: $V_p/V_s = -0.051\phi_{eff} + 2.1775$ and $R^2=0.59$.

1 As for the permeability-porosity relation, especially for facies C, the velocity prediction is not
 2 obvious due to the type and pore structures. Based on the macroscopic description performed
 3 on the 3D images, our samples can be grouped into two classes. On one hand, samples
 4 characterized by micropores and microcracks related to the micritic texture (Fourrier et al.,
 5 2011; Regnet et al., 2019) and on the other hand, vuggy and fractured samples. We found this
 6 segregation on Figure 12a with on the one side the very homogeneous C' facies characterized
 7 by micropores, resulting in low velocities and close to the WTA model. This result was
 8 highlighted by Baechle et al. (2008) and Weger et al. (2009) who showed that carbonate rocks
 9 with more than 80% microporosity have lower velocities for a given porosity. They also showed
 10 that the decrease in the microporosity associated with an increase in the macroporosity leads to
 11 an increase of the velocities. This is the trend we observed in the second cluster composed by
 12 the facies A, B and C. The facies C which is furthermore, the most scattered and the most
 13 heterogeneous facies, appears also as the most weathered facies. Moreover, one could even link
 14 the relative samples weathering (i.e., the proportion of macropores) to the facies discrepancy
 15 observed. Indeed, we have facies C which is the most weathered and the most dispersed in term
 16 of petroacoustic properties, followed by the facies A, the B and finally C', the most
 17 homogenous facies. Conversely to the trend observed for the pore diameters and the
 18 permeability. Indeed, the latter increases with the weathering and the increase of the
 19 macropores.

20 Bulk density effect

21 Figure 13 shows the relationships between saturation V_p and bulk density. Globally, it is difficult
 22 to find any relationship between these two properties. Indeed, there is almost no relationship
 23 between velocities and density as the best fit shows a $R^2=0.4$. It is also the same observation
 24 for V_s . P-wave velocities vary very slightly with bulk density as we probably have a much
 25 greater influence of effective porosity (as shown by the facies C'). On the other side, we have a
 26 greater influence of fractures, cracks and microcracks. Indeed, the effects of these structures
 27 are more preponderant at low effective pressure than at high effective pressure where the
 28 velocity-density relationships are better defined as for the velocity-porosity relationships
 29 (Mavko et al., 1998).

30 The empirical models of Gardner (1974), Castagna & Backus (1993) and Anselmetti & Eberli
 31 (A-E) (1993) were also plotted (equations 4.7 to 4.9). The latter is a modification for high
 32 velocities of Gardner's model which is an average model calibrated over multiple sedimentary
 33 rocks:

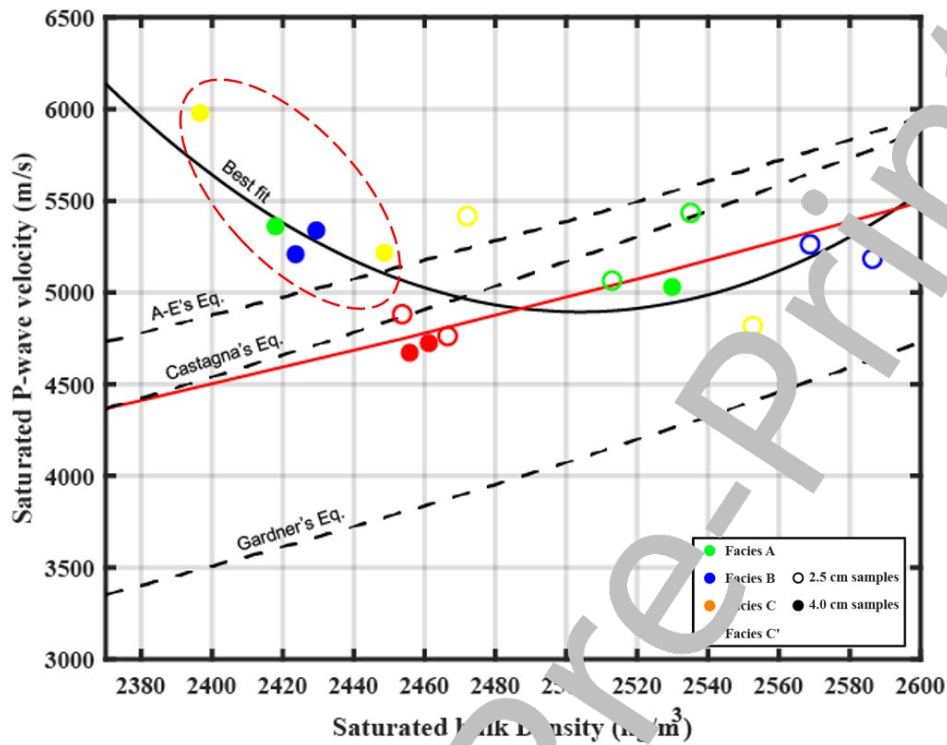
$$34 \quad \rho_b = 1.741V_p^{0.25}, \quad (4.7)$$

$$35 \quad \rho_b = -0.0296V_p^2 + 0.461V_p + 0.963, \quad (4.8)$$

$$36 \quad V_p = 524\rho_b^{2.58}, \quad (4.9)$$

37 where ρ_b is the bulk density (g/cm^3).

38 As we can see the Gardner's model largely underestimates (RMSE=58) our velocities
 39 whatever the facies. Castagna (RMSE=41) and A-E (RMSE=62) models are much better
 40 beyond 2440 kg/m^3 . Below, we have a tendency with a deviation towards high velocities for
 41 low bulk densities materialized by the same particular samples which we have previously
 42 discussed. Not considering them, we found more realistic linear relationships (red line on the
 43 figure) close to Castagna's model.



1

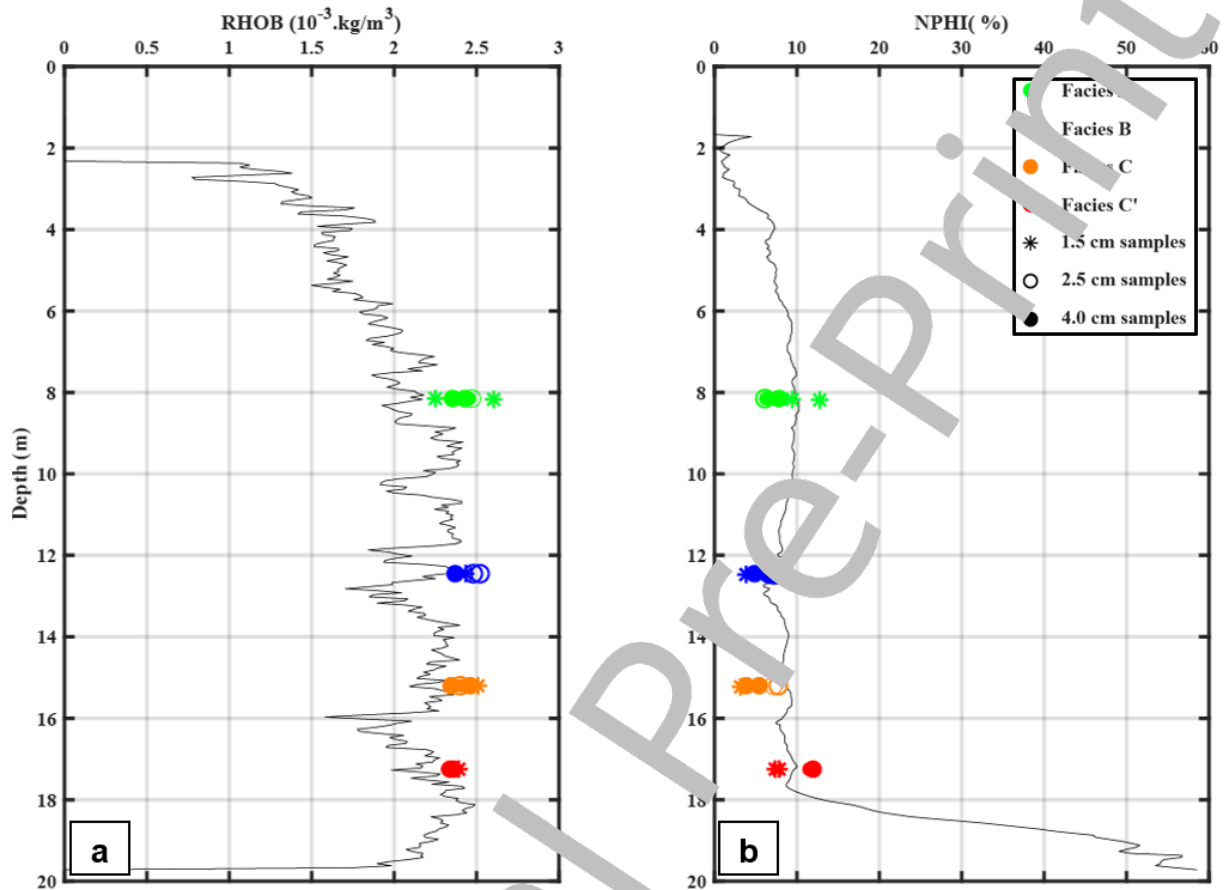
2 Figure 13. Effect of the bulk density on saturated P-wave velocities and three empirical
 3 petroacoustic models (dashed lines for the empirical models of Gardner, 1974, Castagna &
 4 Backus, 1993 and Anselmetti & Eberhart-Phillips, 1993). Bold line: best fit of the plotted data with the
 5 equation: $V_P = 0.0702\rho_b^2 - 351.66\rho_b + 4451.10$ and $R^2 = 0.41$. Red line: regression line of the
 6 plotted data without the five encircled samples with the equation: $V_P = 2.4606\rho_b - 926.85$ and
 7 $R^2 = 0.40$.

8

9 4.5 Size effect: towards an upscaling of the transport properties

10 Figure 14 shows the bulk density and porosity logs, presented by Mallet et al. (2022b), obtained
 11 for Bc8 borehole located in the center of the main well (Figure 1a) where the samples were
 12 taken. By comparing these logs to the laboratory measurements of the different facies, one can
 13 notice a consistency between the laboratory measurements and the logs data, especially for
 14 facies B and C'. In contrast, facies A and C show a relative difference between the two scale of
 15 measurement. Indeed, for facies A, the average density measured in the laboratory is higher
 16 than log's density and the average porosity is almost the same for both laboratory and log
 17 porosity measurement. For facies C, the average density of both measurements is close and the
 18 average effective porosity measured in the laboratory is lower than the log's value. As we
 19 discuss it, the measured discrepancies are linked to the presence of macropores which are more
 20 important for these two facies and tends to control the porosity and the bulk density. Indeed,
 21 2.5 cm diameter samples include relatively a low proportion of macropores whereas for
 22 log data the investigated volume is bigger, therefore including even more macropores as well
 23 as fractures. This could explain the relative low density and high porosity found on the field. This
 24 variation reinforces the observed issue of size (both of sample and observed/considered
 25 heterogeneities). Many authors (Brown et al., 2000; S. Ehrenberg, 2007; Nordahl & Ringrose,
 26 2008; Ringrose et al., 2008; Vik et al., 2013; Bailly et al., 2019) have studied this issue for
 27 reservoir and acoustic properties and its importance for carbonate reservoirs characterization
 28 and upscaling. Thus, our next step for the O-ZNS reservoir modelling is to improve the

- 1 understanding of the size effect by comparing field, log and laboratory (on metric to centimetric
- 2 samples) measurements in order to evaluate how macropores and karsts control at each scale,
- 3 reservoir properties in the VZ as shown in recent study (Flinchum et al., 2022).



4
5 Figure 14. Density (RHOB - A) and Porosity (NPHI - B) logs from the central borehole Bc8
6 compared to the laboratory density and effective porosity measurements.

7
8



1 5 CONCLUSION

2 Petroacoustic characterization of the Beauce limestones, especially for the consolidated part
3 allows obtaining important information for transport properties modelling prior to their
4 integration into a reservoir model in a complex setting such as the vadose zone (multiphase
5 hydrosystem). A total of 24 samples of different structures and different sizes are cored at
6 different depths and analyzed through macroscopic descriptions and petrophysical
7 measurements.

8 Reservoir properties (effective porosity, bulk density, and permeability) are globally scattered
9 and heterogenous, and do not show particular trends with depth. The deepest facies (C'), located
10 at the water table level is the most homogenous one. Comparing petrophysical results to
11 empirical models highlights the effect of mineralogical variations that are related to the
12 presence of detrital minerals due to geochemical and physical weathering of the matrix. We
13 also prove, especially with permeability-porosity relations, the importance of both
14 microporosity linked to the matrices and the macroporosity controlled by fractures, cracks, and
15 vugs. In the case of homogeneous and microporous samples, it is possible to predict their
16 permeability using Kozeny-Carman type models. Conversely, heterogenous samples
17 incorporated macropores are better predicted by Winland's type models, even though they remain
18 difficult to describe and to model. In both cases it is possible to infer the permeability order of
19 magnitude choosing the correct model depending on our pore-structure and size.

20 Regarding the P- and S-wave velocities, the deepest facies is still the most homogeneous with
21 the lowest velocities whether in water saturated or dry conditions. From a general point of view,
22 V_P - V_S relationship is quite difficult to establish and none empirical models yield a good
23 prediction of V_S . We observe that saturating the pore with water tends to homogenize and
24 increase V_P whereas V_S decreases and remains scattered. However, the water saturation effect
25 is very complex to predict and depends on many factors.

26 The primary control of the elastic properties is the porosity which results in a decrease in
27 velocities when the effective porosity increases, especially for V_P even though some
28 discrepancies are observed. These discrepancies are linked to the pore structure of which
29 macropores tends to scatter values and minimize the control of the effective porosity. Finally,
30 by applying petroacoustic models, we were able to demonstrate close relationship between pore
31 type, structure and petroacoustic properties. This may be a tool for carbonate facies
32 discrimination and can be used to improved fluid flow simulation models in the vadose zone.
33 However, further development is needed in order to assess the size effect and permeability
34 models using electrical methods.

35

36



1 REFERENCES

- 2 Abbar, B., Isch, A., Michel, K., Abbas, M., Vincent, H., Abbasimaedeh, P., & Azaroual, M. (2022). Fiber
3 optic technology for environmental monitoring: State of the art and application in the
4 observatory of transfers in the Vadose Zone-(O-ZNS). *Instrumentation and Measurement
5 Technologies for Water Cycle Management*, 189–222. [https://doi.org/10.1007/978-3-031-](https://doi.org/10.1007/978-3-031-08262-7_9)
6 [08262-7_9](https://doi.org/10.1007/978-3-031-08262-7_9)
- 7 Abbas, M., Deparis, J., Isch, A., Mallet, C., Jodry, C., Azaroual, M., Abbar, B., & Baudouin, J. (2022).
8 Hydrogeophysical characterization and determination of petrophysical parameters by
9 integrating geophysical and hydrogeological data at the limestone vadose zone of the Beauce
10 aquifer. *Journal of Hydrology*, 615, 128725. <https://doi.org/10.1016/j.jhydrol.2022.128725>
- 11 Aldana, C., Isch, A., Bruand, A., Azaroual, M., & Coquet, Y. (2021). Relationship between hydraulic
12 properties and material features in a heterogeneous vadose zone of a vulnerable limestone
13 aquifer. *Vadose Zone Journal*, 20(4), e20127. <https://doi.org/10.1002/vzj2.20127>
- 14 Amyx, J. W., Bass Jr, D. M., & Whiting, R. L. (1960). *Petroleum reservoir engineering: Physical properties*.
15 McGraw-Hill Inc. ISBN 9780070016002
- 16 Anselmetti, F. S., & Eberli, G. P. (1993). Controls on sonic velocity in carbonates. *Pure and Applied
17 Geophysics*, 141, 287–323. <https://doi.org/10.1007/BF00600233>
- 18 API. (1998). *Recommended practices for core analysis* (2nd ed.). Washington DC: American Petroleum
19 Institute. <https://www.energistics.org/sites/default/files/2022-10/rp40.pdf>
- 20 Archie, G. E. (1950). Introduction to petrophysics of reservoir rocks. *AAPG Bulletin*, 34(5), 943–961.
21 <https://doi.org/10.1306/3D933F62-16B1-11D7-8645000102C1865D>
- 22 Assefa, S., McCann, C., & Sothcott, J. (2003). Velocities of compressional and shear waves in
23 limestones. *Geophysical Prospecting*, 51(1), 1–13. [https://doi.org/10.1046/j.1365-](https://doi.org/10.1046/j.1365-2478.2003.00349.x)
24 [2478.2003.00349.x](https://doi.org/10.1046/j.1365-2478.2003.00349.x)
- 25 Baechle, G. T., Colpaert, A., Eberli, G. P., & Weger, R. J. (2002). Effects of microporosity on sonic velocity
26 in carbonate rocks. *The Leading Edge*, 27(8), 1012–1018. <https://doi.org/10.1190/1.2967554>
- 27 Bailly, C., Kernif, T., Hamon, Y., Adelinet, M., & Fortin, J. (2022). Controlling factors of acoustic
28 properties in continental carbonates: Implications for high-resolution seismic imaging. *Marine
29 and Petroleum Geology*, 137, 105518. <https://doi.org/10.1016/j.marpetgeo.2021.105518>
- 30 Beck, K., & Al-Mukhtar, M. (2010). Weathering effects in an urban environment: A case study of
31 tuffeau, a French porous limestone. *Geological Society, London, Special Publications*, 331(1),
32 103–111. <https://doi.org/10.1144/SP331.8>
- 33 Berg, R. R. (1970). Method for determining permeability from reservoir rock properties. *Transactions,
34 Gulf Coast Association of Geological Societies*, 20, 303–317.
- 35 Bernabé, Y., & Maineult, A. (2011). 11.02 - Physics of Porous Media: Fluid Flow Through Porous.
36 *Treatise on Geophysics (Second Edition)*, 19-41. [Mediahttps://doi.org/10.1016/B978-0-444-](https://doi.org/10.1016/B978-0-444-53802-4.00188-3)
37 [53802-4.00188-3](https://doi.org/10.1016/B978-0-444-53802-4.00188-3)
- 38 Binley, A., Hubbard, S. S., Huisman, J. A., Revil, A., Robinson, D. A., Singha, K., & Slater, L. D. (2015). The
39 emergence of hydrogeophysics for improved understanding of subsurface processes over
40 multiple scales. *Water Resources Research*, 51(6), 3837–3866.
41 <https://doi.org/10.1002/2015WR017016>
- 42 Biot, M. A. (1956). Theory of propagation of elastic waves in a fluid-saturated porous solid. II. Higher
43 frequency range. *The Journal of the Acoustical Society of America*, 28(2), 179–191.
44 <https://doi.org/10.1121/1.1908241>
- 45 Block, S. (1951). Empirical prediction of porosity and permeability in sandstones. *AAPG Bulletin*, 75(7),
46 1145–1160. <https://doi.org/10.1306/OC9B28E9-1710-11D7-8645000102C1865D>
- 47 Boussock, D., Potten, M., Pfrang, D., Wolpert, P., & Zosseder, K. (2020). Porosity–permeability
48 relationship derived from Upper Jurassic carbonate rock cores to assess the regional hydraulic
49 matrix properties of the Malm reservoir in the South German Molasse Basin. *Geothermal
50 Energy*, 8(1), 1–47. <https://doi.org/10.1186/s40517-020-00166-9>



- 1 Bosch, M., Mukerji, T., & Gonzalez, E. F. (2010). Seismic inversion for reservoir properties combining
2 statistical rock physics and geostatistics: A review. *Geophysics*, 75(5), 75A1–75A176.
3 <https://doi.org/10.1190/1.3478209>
- 4 Bourbié, T., Coussy, O., Zinszner, B., & Junger, M. C. (1992). *Acoustics of porous media*. Acoustical
5 Society of America. ISBN 2710805162978
- 6 Brown, G., Hsieh, H., & Lucero, D. A. (2000). Evaluation of laboratory dolomite core sample size using
7 representative elementary volume concepts. *Water Resources Research*, 36(5), 1199–1207.
8 <https://doi.org/10.1029/2000WR900017>
- 9 Cadoret, T., Marion, D., & Zinszner, B. (1995). Influence of frequency and fluid distribution on elastic
10 wave velocities in partially saturated limestones. *Journal of Geophysical Research: Solid Earth*,
11 100(B6), 9789–9803. <https://doi.org/10.1029/95JB00757>
- 12 Cardona, A., & Santamarina, J. C. (2020). Carbonate rocks: Matrix permeability estimation. *AAPG*
13 *Bulletin*, 104(1), 131–144. <https://doi.org/10.1306/05021917345>
- 14 Carman, P. C. (1997). Fluid flow through granular beds. *Chemical Engineering Research and Design*, 75,
15 S32–S48. [https://doi.org/10.1016/S0263-8762\(97\)80003-2](https://doi.org/10.1016/S0263-8762(97)80003-2)
- 16 Castagna, J. P., & Backus, M. M. (1993). *Offset-dependent reflectivity—Theory and practice of AVO*
17 *analysis*. Society of Exploration Geophysicists. ISBN 978150080262
- 18 Castagna, J. P., Batzle, M. L., & Eastwood, R. L. (1985). Relationships between compressional-wave and
19 shear-wave velocities in clastic silicate rocks. *Geophysics*, 50(4), 571–581.
20 <https://doi.org/10.1190/1.1441933>
- 21 Chilingar, G. V. (1964). Relationship between porosity, permeability, and grain-size distribution of
22 sands and sandstones. In *Developments in sedimentology*, 1, 71–75.
23 [https://doi.org/10.1016/S0070-4571\(08\)70411-2](https://doi.org/10.1016/S0070-4571(08)70411-2)
- 24 Choquette, P. W., & Pray, L. C. (1970). Geologic nomenclature and classification of porosity in
25 sedimentary carbonates. *AAPG Bulletin*, 54(2), 207–250. [https://doi.org/10.1306/5D25C98B-](https://doi.org/10.1306/5D25C98B-16C1-11D7-8645000102C1865D)
26 [16C1-11D7-8645000102C1865D](https://doi.org/10.1306/5D25C98B-16C1-11D7-8645000102C1865D)
- 27 Domenico, S. (1976). Effect of brine-gas mixture on velocity in an unconsolidated sand reservoir.
28 *Geophysics*, 41(5), 882–894. <https://doi.org/10.1190/1.1440670>
- 29 Dominguez, G., Samaniego, FV, Mazzullo, S, Rieke, HH, & Chilingarian, GV. (1992). *Carbonate reservoir*
30 *characterization: A geologic engineering analysis, Part I*. Elsevier. ISBN 9780080868882
- 31 Dunham, R. J. (1962). Classification of carbonate rocks according to depositional textures. *AAPG Special*
32 *Volumes*, 180–121. ISBN 0781629812366
- 33 Ehrenberg, S. (2007). Whole core versus plugs: Scale dependence of porosity and permeability
34 measurements in platform carbonates. *AAPG Bulletin*, 91(6), 835–846.
35 <https://doi.org/10.1306/01000706093>
- 36 Ehrenberg, S., & Nadeau, P. (2005). Sandstone vs. Carbonate petroleum reservoirs: A global
37 perspective on porosity-depth and porosity-permeability relationships. *AAPG Bulletin*, 89(4),
38 435–445. <https://doi.org/10.1306/11230404071>
- 39 Fabricius, I. L., Buchle, G. T., & Eberli, G. P. (2010). Elastic moduli of dry and water-saturated
40 carbonates—Effect of depositional texture, porosity, and permeability. *Geophysics*, 75(3),
41 N65–N78. <https://doi.org/10.1190/1.3374690>
- 42 Fabricius, I. L., Buchle, G., Eberli, G. P., & Weger, R. (2007). Estimating permeability of carbonate rocks
43 from porosity and vp/vs. *Geophysics*, 72(5), E185–E191. <https://doi.org/10.1190/1.2756081>
- 44 Fan, B., Liu, J., Zhu, Q., Qin, G., Li, J., Lin, H., & Guo, L. (2020). Exploring the interplay between
45 infiltration dynamics and Critical Zone structures with multiscale geophysical imaging: A
46 review. *Geoderma*, 374, 114431. <https://doi.org/10.1016/j.geoderma.2020.114431>
- 47 Flinchum, B. A., Holbrook, W. S., & Carr, B. J. (2022). What Do P-Wave Velocities Tell Us About the
48 Critical Zone? *Frontiers in Water*, 3, 772185. <https://doi.org/10.3389/frwa.2021.772185>
- 49 Folk, R. L. (1959). Practical petrographic classification of limestones. *AAPG Bulletin*, 43(1), 1–38.
50 <https://doi.org/10.1306/0BDA5C36-16BD-11D7-8645000102C1865D>



- 1 Fournier, F., Leonide, P., Biscarrat, K., Gallois, A., Borgomano, J., & Foubert, A. (2011). Elastic properties
2 of microporous cemented grainstones. *Geophysics*, 76(6), E1–E226.
3 <https://doi.org/10.1190/geo2011-0047.1>
- 4 Gardner, G., Gardner, L., & Gregory, Ar. (1974). Formation velocity and density—The diagnostic basics
5 for stratigraphic traps. *Geophysics*, 39(6), 770–780. <https://doi.org/10.1190/1.440465>
- 6 Gassmann, F. (1951). Elastic waves through a packing of spheres. *Geophysics*, 16(4), 673–685.
7 <https://doi.org/10.1190/1.1437718>
- 8 Germán Rubino, J., Guarracino, L., Müller, T. M., & Holliger, K. (2013). Do seismic waves sense fracture
9 connectivity? *Geophysical Research Letters*, 40(4), 692–696.
10 <https://doi.org/10.1002/grl.50127>
- 11 Greenberg, M., & Castagna, J. (1992). Shear-wave velocity estimation in porous rocks: Theoretical
12 formulation, preliminary verification and applications1. *Geophysical Prospecting*, 40(2), 195–
13 209. <https://doi.org/10.1111/j.1365-2478.1992.tb00371.x>
- 14 Guéguen, Y., Sarout, J., Fortin, J., & Schubnel, A. (2009). Cracks in porous rocks: Tiny defects, strong
15 effects. *The Leading Edge*, 28(1), 40–47. <https://doi.org/10.1190/1.3064145>
- 16 Han, D., Nur, A., & Morgan, D. (1986). Effects of porosity and cementation content on wave velocities in
17 sandstones. *Geophysics*, 51(11), 2093–2107. <https://doi.org/10.1190/1.1442062>
- 18 Hermans, T., Goderniaux, P., Jougnot, D., Fleckenstein, J. H., Brunner, P., Nguyen, F., Linde, N.,
19 Huisman, J. A., Bour, O., Lopez Alvis, J., & others. (2023). Advancing measurements and
20 representations of subsurface heterogeneity and dynamic processes: Towards 4D
21 hydrogeology. *Hydrology and Earth System Sciences*, 27(1), 255–287.
22 <https://doi.org/10.5194/hess-27-255-2023>
- 23 Isch, A., Coquet, Y., Abbar, B., Aldana, C., Abbas, M., Bruand, A., & Azaroual, M. (2022). A
24 comprehensive experimental and numerical analysis of water flow and travel time in a highly
25 heterogeneous vadose zone. *Journal of Hydrology*, 610, 127875.
26 <https://doi.org/10.1016/j.jhydrol.2022.127875>
- 27 Jaya, I., Sudaryanto, A., & Widarsono, B. (2005). Permeability prediction using pore throat and rock
28 fabric: A model from Indonesian reservoirs. *SPE Asia Pacific Oil and Gas Conference and
29 Exhibition*, SPE-93363. <https://doi.org/10.2118/93363-MS>
- 30 Kearey, P., Brooks, M., & Hill, I. (2002). *An introduction to geophysical exploration*. John Wiley & Sons.
31 ISBN 9781118698938
- 32 Kolodzie Jr, S. (1980). Analysis of pore throat size and use of the Waxman-Smits equation to determine
33 OOIP in Spindle Field, Colorado. *SPE Annual Technical Conference and Exhibition?*, SPE-9382.
34 <https://doi.org/10.2118/9382-MS>
- 35 Lake, L. (2012). *Reservoir characterization* (1st ed.). Elsevier. ISBN 9780323143516
- 36 Laurent, G., Mallet, C., Dewett, T., François, L., Abbar, B., Abbas, M., & Azaroual, M. (2023). *Digital
37 Outcrop Acquisition for the Observatory of the Vadose Zone (OZNS)* (EGU23-15336). EGU23.
38 Copernicus Meetings. <https://doi.org/10.5194/egusphere-egu23-15336>
- 39 Lebedev, M., Tom Stewart, J., Clennell, B., Pervukhina, M., Shulakova, V., Paterson, L., Müller, T. M.,
40 Gurevich, V., & Wenzlau, F. (2009). Direct laboratory observation of patchy saturation and its
41 effects on ultrasonic velocities. *The Leading Edge*, 28(1), 24–27.
42 <http://doi.org/10.1190/1.3064142>
- 43 Leroy, P., Hardt, A., Gboreau, S., Zimmermann, E., Claret, F., Bucker, M., Stebner, H., & Huisman, J. A.
44 (2019). Spectral induced polarization of low-pH cement and concrete. *Cement and Concrete
45 Composites*, 104, 103397. <https://doi.org/doi:10.1016/j.cemconcomp.2019.103397>
- 46 Lovat, A. (2006). Making sense of carbonate pore systems. *AAPG Bulletin*, 90(9), 1381–1405.
47 <https://doi.org/10.1306/03130605104>
- 48 Lorain, J.-M. (1973). *La géologie du calcaire de Beauce*. Paris: Laboratoire central des Ponts et
49 Chaussées.
- 50 Lucia, F. J. (1983). Petrophysical parameters estimated from visual descriptions of carbonate rocks: A
51 field classification of carbonate pore space. *Journal of Petroleum Technology*, 35(03), 629–637.
52 <https://doi.org/10.2118/10073-PA>



- 1 Lucia, F. J. (1995). Rock-fabric/petrophysical classification of carbonate pore space for reservoir
2 characterization. *AAPG Bulletin*, 79(9), 1275–1300. [https://doi.org/10.1306/7834B4A4-1721-](https://doi.org/10.1306/7834B4A4-1721-11D7-8645000102C1865D)
3 [11D7-8645000102C1865D](https://doi.org/10.1306/7834B4A4-1721-11D7-8645000102C1865D)
- 4 Lucia, F. J. (2007). *Carbonate Reservoir Characterization*. Springer Berlin Heidelberg.
5 <https://doi.org/10.1007/978-3-540-72742-2>
- 6 Mallet, C., Isch, A., Laurent, G., Jodry, C., & Azaroual, M. (2022a). Integrated static and dynamic
7 geophysical and geomechanical data for characterization of transport properties. *International*
8 *Journal of Rock Mechanics and Mining Sciences*, 152, 105050.
9 <https://doi.org/10.1016/j.ijrmms.2022.105050>
- 10 Mallet, C., Jodry, C., Isch, A., Laurent, G., Deparis, J., & Azaroual, M. (2022b). Multi-geophysical field
11 measurements to characterize lithological and hydraulic properties of a multi-scale karstic and
12 fractured limestone vadose zone: Beauce aquifer (France). In *Instrumentation and*
13 *Measurement Technologies for Water Cycle Management*, 461–484.
14 <https://doi.org/10.1007/978-3-031-08262-7>
- 15 Mavko, G., Mukerji, T., & Dvorkin, J. (1998). *The rock physics handbook* (1st ed.). Cambridge university
16 press. <https://doi.org/10.1017/CBO9780511626753>
- 17 Ménillet, F., & Edwards, N. (2000). The Oligocene-Miocene Calcaires de Beauce (Beauce Limestones),
18 Paris Basin, France. In *Lake basins through space and time*. *AAPG Studies in Geology*, 46, 417–
19 424. <https://doi.org/10.1306/St46706C38>
- 20 Miaomiao, L., Benbiao, S., Changbing, T., & Xianyu, M. (2021). Relationship between pore throat and
21 permeability of porous carbonate reservoir in the Middle East. *Arabian Journal of Geosciences*,
22 15, 1–7. <https://doi.org/10.1007/s12517-021-08162-9>
- 23 Moore, C. H., & Wade, W. J. (2002). *Carbonate Reservoirs: Porosity and diagenesis in a sequence*
24 *stratigraphic framework* (1st ed.). Newnes. ISBN 044538313
- 25 National Research Council. (2001). *Basic Research Opportunities in Earth Science*. The National
26 Academies Press. <https://doi.org/10.17226/9981>
- 27 Nelson, P. H. (1994). Permeability-porosity relationships in sedimentary rocks. *The Log Analyst*, 35(03),
28 38–62.
- 29 Nordahl, K., & Ringrose, P. S. (2008). Identifying the representative elementary volume for
30 permeability in heterolithic deposits using numerical rock models. *Mathematical Geosciences*,
31 40(7), 753–771. <https://doi.org/10.1007/s11004-008-9182-4>
- 32 Palaz, I., & Marfurt, K. J. (1997). *Carbonate seismology*. Society of Exploration Geophysicists. ISBN
33 9781560802099
- 34 Panza, E., Agosta, F., Rustichelli, A., Vinciguerra, S., Ougier-Simonin, A., Dobbs, M., & Prosser, G. (2019).
35 Meso-to-microscale fracture porosity in tight limestones, results of an integrated field and
36 laboratory study. *Marine and Petroleum Geology*, 103, 581–595.
37 <https://doi.org/10.1016/j.marpetgeo.2019.01.043>
- 38 Pickett, G. R. (1963). Sonic character logs and their applications in formation evaluation. *Journal of*
39 *Petroleum Technology*, 15(06), 659–667. <https://doi.org/10.2118/452-PA>
- 40 Pittman, E. D. (2002). Relationship of porosity and permeability to various parameters derived from
41 mercury injection-capillary pressure curves for sandstone. *AAPG Bulletin*, 76(2), 191–198.
42 <https://doi.org/10.1306/BDF87A4-1718-11D7-8645000102C1865D>
- 43 Rafavich, F., Kendall, C. S. C., & Todd, T. (1984). The relationship between acoustic properties and the
44 petrographic character of carbonate rocks. *Geophysics*, 49(10), 1622–1636.
45 <https://doi.org/10.1190/1.1441570>
- 46 Renolff-Jaon, P., & Zinszner, B. (2004). Laboratory petroacoustics for seismic monitoring feasibility
47 study. *The Leading Edge*, 23(3), 252–258. <https://doi.org/10.1190/1.1690898>
- 48 Raymer, L. W., Hunt, E. R., & Gardner, J. S. (1980). An improved sonic transit time-to-porosity transform.
49 *SPWLA Annual Logging Symposium*, 1–13.
- 50 Regnet, J.-B., David, C., Robion, P., & Menéndez, B. (2019). Microstructures and physical properties in
51 carbonate rocks: A comprehensive review. *Marine and Petroleum Geology*, 103, 366–376.
52 <https://doi.org/10.1016/j.marpetgeo.2019.02.022>



- 1 Regnet, J.-B., Robion, P., David, C., Fortin, J., Brigaud, B., & Yven, B. (2015). Acoustic and reservoir
2 properties of microporous carbonate rocks: Implication of micrite particle size and
3 morphology. *Journal of Geophysical Research: Solid Earth*, 120(2), 75–81.
4 <https://doi.org/10.1002/2014JB011313>
- 5 Rembert, F., Léger, M., Jougnot, D., & Luquot, L. (2023). Geoelectrical and hydro-chemical monitoring
6 of karst formation at the laboratory scale. *Hydrology and Earth System Sciences*, 27(2), 417–
7 430. <http://dx.doi.org/10.5194/hess-27-417-2023>
- 8 Rezaee, M., Jafari, A., & Kazemzadeh, E. (2006). Relationships between permeability, porosity and pore
9 throat size in carbonate rocks using regression analysis and neural networks. *Journal of*
10 *Geophysics and Engineering*, 3(4), 370–376. <https://doi.org/10.1098/1747-1021/3/4/008>
- 11 Ringrose, P. S., Martinius, A. W., & Alvestad, J. (2008). Multiscale geological reservoir modelling in
12 practice. *Geological Society, London, Special Publications*, 309(1), 123–134.
13 <https://doi.org/10.1144/SP309.9>
- 14 Stephens, D. B. (1996). *Vadose zone hydrology* (1st ed.). CRC press.
15 <https://doi.org/10.1201/9780203734490>
- 16 Tatham, R. H. (1982). V p V s and lithology. *Geophysics*, 47(3), 336–344.
17 <https://doi.org/10.1190/1.1441339>
- 18 Tiab, D., & Donaldson, E. C. (2015). *Petrophysics: Theory and practice of measuring reservoir rock and*
19 *fluid transport properties* (4th ed.). Gulf professional publishing.
20 <https://doi.org/10.1016/C2014-0-03707-0>
- 21 Trautmann, F. (1974). *Les formations du groupe de Beaune: Caractéristiques et Utilisations*. Bureau de
22 Recherches Géologiques et Minières (BRGM). [http://infoterre.brgm.fr/rapports/74-SGN-358-](http://infoterre.brgm.fr/rapports/74-SGN-358-BSS.pdf)
23 [BSS.pdf](http://infoterre.brgm.fr/rapports/74-SGN-358-BSS.pdf)
- 24 Tucker, M. E., & Wright, V. P. (2009). *Carbonate sedimentology*. John Wiley & Sons.
25 DOI:10.1002/9781444314175
- 26 United Nations. (2022). *The United Nations World Water Development Report 2022: Groundwater:*
27 *Making the invisible visible*. Paris: UNESCO.
28 <https://unesdoc.unesco.org/ark:/48223/pf0000380721>
- 29 Vernik, L., & Nur, A. (1992). Petrophysical classification of siliciclastics for lithology and porosity
30 prediction from seismic velocities. *AAPG Bulletin*, 76(9), 1295–1309.
31 <https://doi.org/10.1306/B0FF89C0-1718-11D7-8645000102C1865D>
- 32 Verwer, K., Braaksma, H., & Keeler, J. A. (2008). Acoustic properties of carbonates: Effects of rock
33 texture and implications for fluid substitution. *Geophysics*, 73(2), B51–B65.
34 <https://doi.org/10.1190/1.27831935>
- 35 Vik, B., Bastesen, E., & Skauge, A. (2013). Evaluation of representative elementary volume for a vuggy
36 carbonate rock—Part I: Porosity, permeability, and dispersivity. *Journal of Petroleum Science*
37 *and Engineering*, 112, 36–47. <https://doi.org/10.1016/j.petrol.2013.03.029>
- 38 Wang, Z., Hirsche, V. K., & Hedgwick, G. (1991). Seismic velocities in carbonate rocks. *Journal of*
39 *Canadian Petroleum Technology*, 30(02), PETSOC-91-02-09. <https://doi.org/10.2118/91-02-09>
- 40 Webb, P. A. (2001). An introduction to the physical characterization of materials by mercury intrusion
41 porosimetry, with emphasis on reduction and presentation of experimental data. *Micromeritics*
42 *Instrumentation Corp*, Norcross.
43 https://mail.micromeritics.com/Repository/Files/mercury_paper.pdf
- 44 Wegner, R. J., Berli, G. P., Baechle, G. T., Massaferro, J. L., & Sun, Y.-F. (2009). Quantification of pore
45 structure and its effect on sonic velocity and permeability in carbonates. *AAPG Bulletin*, 93(10),
46 1297–1317. <https://doi.org/10.1306/05270909001>
- 47 Wyllie, M. R. J., Gregory, A. R., & Gardner, L. W. (1956). Elastic wave velocities in heterogeneous and
48 porous media. *Geophysics*, 21(1), 41–70. <https://doi.org/10.1190/1.1438217>
- 49 Yu, X., Li, S., & Li, S. (2018). *Clastic hydrocarbon reservoir sedimentology*. Springer.
50 <https://doi.org/10.1007/978-3-319-70335-0>
- 51 Zinszner, B., & Pellerin, F.-M. (2007). *A geoscientist's guide to petrophysics* (1st ed.). Editions Technip.
52 ISBN 2710808994



1 **APPENDIX**

2 Table 1. Description of the different samples and characterization method

Code	Facies	Depth (m)	Nb of samples	Diameter (cm)	Length (cm)	Characterization method
A20	A	7.80-8.50	2	1.49	1.65	Mercury injection
A25	A	7.80-8.50	2	2.50	5.00	Porosity permeability acoustics
A40	A	7.80-8.50	2	4.00	9.80	
B20	B	11.80-13.10	2	1.46	1.72	Mercury injection
B25	B	11.80-13.10	2	2.50	4.70	Porosity permeability acoustics
B40	B	11.80-13.10	2	4.00	10.05	
C20	C	14.50-15.90	2	1.45	1.71	Mercury injection
C25	C	14.50-15.90	2	2.50	5.10	Porosity permeability Acoustics
C40	C	14.50-15.90	2	4.00	10.10	
C'20	C'	17.0-17.50	2	1.44	1.78	Mercury injection
C'25	C'	17.0-17.50	2	2.50	5.30	Porosity permeability acoustics
C'40	C'	17.0-17.50	2	4.00	10.40	

3

4



1 **ACKNOWLEDGMENTS**

2 This research work was conducted within the framework of the O-ZNS project which is part of
3 the regional program PIVOTS. We gratefully acknowledge the financial support provided by
4 the Region Centre-Val de Loire (ARD 2020 program and CPER 2015 -2020) and the French
5 Ministry of Higher Education and Research (CPER 2015 -2020 and public service to BRGM).
6 This is also co-funded by European Union with the European Regional Development Fund
7 (FEDER). Finally, this research work is co-funded by the Labex VOLTAIRE (ANR-10-LABX-

8

9 **DATA AVAILABILITY STATEMENT**

10 The data that supports the findings of this study are available upon request from corresponding
11 authors. In addition, they will be soon available on the public repository of the O-ZNS
12 observatory with their own DOI.

13